A&A 467, 565–584 (2007)
DOI: 10.1051/0004-6361:20066795

Astronomy & Astrophysics

Keck spectroscopy of $z = 1$–3 ULIRGs from the Spitzer SWIRE survey⋆,⋆⋆

S. Berta[1,2,⋆⋆⋆], C. J. Lonsdale[2,3], B. Siana[4], D. Farrah[5], H. E. Smith[2], M. C. Polletta[2], A. Franceschini[1], J. Fritz[1,6], I. Perez-Fournon[7], M. Rowan-Robinson[8], D. Shupe[4], and J. Surace[4]

[1] Dipartimento di Astronomia, Università di Padova, Vicolo dell'Osservatorio 2, 35122 Padova, Italy
e-mail: berta@pd.astro.it, ste_atreb@yahoo.it
[2] Center for Astrophysics and Space Sciences, University of California, San Diego, 9500 Gilman Dr., La Jolla, CA 92093-0424, USA
[3] Infrared Processing & Analysis Center, California Institute of Technology 100-22, Pasadena, CA 91125, USA
[4] Spitzer Science Center, California Institute for Technology, 220-6, Pasadena, CA 91125, USA
[5] Astronomy Department, Cornell University, Itaca, NY 14853, USA 100-22, Pasadena, CA 91125, USA
[6] INAF Osservatorio Astronomico di Bologna, via Ranzani 1, 40127 Bologna, Italy
[7] Instituto de Astrofisica de Canarias, 38200 La Laguna, Tenerife, Spain
[8] Astrophysics Group, Blackett Laboratory, Imperial College London, Prince Consort Road, London SW7 2BW, UK

Received 22 November 2006 / Accepted 8 March 2007

ABSTRACT

Context. High-redshift ultra luminous infrared galaxies contribute the bulk of the cosmic IR background and are the best candidates for very massive galaxies in formation at $z > 1.5$.

Aims. It is necessary to identify the energy source for their huge luminosities, starburst or AGN activity, in order to correctly interpret the role of ULIRGs in galaxy evolution, and compute reliable estimates of their star formation rates, stellar masses, and accretion luminosities.

Methods. We present Keck/LRIS optical spectroscopy of 35 $z \geq 1.4$ luminous IR galaxies in the Spitzer Wide-area Infra-Red Extragalactic survey (SWIRE) northern fields (Lockman Hole, ELAIS-N1, ELAIS-N2). The primary targets belong to the "IR-peak" class of galaxies, having the 1.6 μm (restframe) stellar feature detected in the IRAC Spitzer channels. The spectral energy distributions of the main targets are thoroughly analyzed, by means of spectro-photometric synthesis and multi-component fits (stars + starburst dust + AGN torus).

Results. The IR-peak selection technique is confirmed to successfully select objects above $z = 1.4$, though some of the observed sources lie at lower redshift than expected. Among the 16 galaxies with spectroscopic redshift, 62% host an AGN component, two thirds being type-1 and one third type-2 objects. The selection, limited to $r' < 24.5$, is likely biased to optically-bright AGNs. All IR-peakers without emission lines have a non negligible continuum detection, and are likely to be very powerful starbursts, heavily extinguished by dust ($A_V \geq 5$ mag). The SEDs of non-AGN IR-peakers resemble those of starbursts (SFR = 20–500 $M_\odot$/yr) hosted in massive ($M > 10^{11}$ $M_\odot$) galaxies. The presence of an AGN component provides a plausible explanation for the spectroscopic/photometric redshift discrepancies, as the torus produces an apparent shift of the peak to longer wavelengths. These sources are analyzed in IRAC and optical-IR color spaces. In addition to the IR-peak galaxies, we present redshifts and spectral properties for 150 objects, out of a total of 301 sources on slits.

Key words. galaxies: distance and redshifts – galaxies: active – galaxies: starburst – galaxies: high redshift – galaxies: fundamental parameters – infrared: galaxies

1. Introduction: distant starbursts in the SWIRE survey

Locally rare, Ultra-luminous ($L_{IR} > 10^{12}$ $L_\odot$, ULIRGs) and Hyper-luminous ($L_{IR} > 10^{13}$ $L_\odot$, HLIRGs) infrared galaxies dominate the energy budget in the distant Universe (e.g. Franceschini et al. 2001; Elbaz et al. 2002).

Extragalactic surveys with ISO, SCUBA, MAMBO[1] (e.g. Franceschini et al. 2003; Genzel & Cesarsky, 2000; Ivison et al. 1998; see Lonsdale et al. 2006, for a review), and now *Spitzer* have shown that the number of dusty, IR-luminous galaxies at $2 < z < 3$ is several orders of magnitude higher than in the local Universe. The analysis of the statistical properties of high-z ULIRGs has shown that they contribute substantially to the cosmic infrared background (CIRB), discovered by COBE in the late '90s (Puget et al. 1996; Hauser et al. 1998; Elbaz et al. 2002; Dole et al. 2006).

The currently most successful models for galaxy formation all invoke a "biased" hierarchical buildup within a ΛCDM

⋆ Based on data obtained at the W. M. Keck Observatory, which is operated as a scientific partnership between the California Institute of Technology, the University of California, and NASA, and made possible by the generous financial support of the W. M. Keck Foundation.

⋆⋆ Tables 5, 6 and Fig. 7 are only available in electronic form at http://www.aanda.org

⋆⋆⋆ S.B. was supported by the Ing. Aldo Gini Foundation

[1] Distant ULIRGs are commonly referred to as submillimeter galaxies, or SMGs; here we reserve that term explicitly for systems selected in submm or mm surveys, because distant ULIRGs selected at other wavelengths may not necessarily be (sub)mm-luminous.

cosmology (e.g. Cole et al. 2000; Hatton et al. 2003; Granato et al. 2004) to assemble galaxies, suggesting that the most massive objects (e.g. $M_{\rm stars} >$ several 10^{11} $M_\odot$) may assemble earlier, more quickly and in richer environments than less massive ones. This may occur in short-lived, intense bursts of star formation at $z > 2$ (Somerville et al. 2001; Nagamine et al. 2005). This theoretical framework has enjoyed great success in describing many observational results from the local Universe, and at moderate redshifts (e.g. Cole et al. 2005).

The sternest tests of these models, however, come from observations at $z > 1$, where the earliest formation stages of massive galaxies and rich clusters are predicted to occur. Several pieces of evidence exist that fully formed massive galaxies were already in place at redshift $z > 1.5$ (e.g. Ellis et al. 1997; van Dokkum et al. 2003).

Analyses of the ultra-luminous submillimeter galaxy (SMG) population at $z > 1.5$ (e.g. Chapman et al. 2004) support extreme star-formation rates in rare massive objects. These distant IR sources, with implied $SFR > 500$ $M_\odot$/yr (e.g. Farrah et al. 2002), are the best candidates to be the progenitors of ellipticals which formed most of their stars rapidly at $z \sim 2$–4.

Nevertheless, whether the huge luminosities of ULIRGs and SMGs are powered by starburst emission, AGN accretion or a combination of the two has been often, and is still, a matter of debate. Discriminating between starburst and AGN power is fundamentally important for properly measuring their star formation rates, stellar masses, accretion rates, and also for understanding the connection between bulge and black hole building.

Spitzer (Werner et al. 2004) holds the key to this major question, because the IR broadband spectral energy distributions (SEDs) and IRS (Houck et al. 2004) spectra of $z > 1$ sources can discriminate warm AGN-dominated emission, characterized by a power-law (torus-like) SEDs, from emission dominated by stars (e.g. Weedman et al. 2006). Lacy et al. (2004) and Stern et al. (2005) have demonstrated a strong segregation of AGN-dominated systems from starburst-dominated galaxies in the IRAC color-color space.

The first major IRS surveys of the 24 μm-brightest, optically-faint galaxies from Spitzer surveys have shown that they tend to be dominated by warm AGN-heated dust (Houck et al. 2005; Yan et al. 2005). Polletta et al. (2006) and Lonsdale et al. (in prep.) have used the added power of SED analysis to distinguish the main energy source and estimate photometric redshifts for high redshift ULIRGs in the *Spitzer Wide-area InfraRed Extragalactic* Legacy survey (SWIRE Lonsdale et al. 2003, 2004), and find that the AGN/starburst fraction decreases rapidly with decreasing 24 μm flux, until starburst-dominated systems far exceed AGN-dominated ones as f_{24} drops below 500 μJy (Lonsdale et al.). Weedman et al. (2006) have confirmed these broadband AGN vs. starburst classifications, by exploiting IRS spectroscopy of 17 $z \sim 2$ ULIRGs and finding that the broadband classifications are correct in 90% of the cases.

Finally, Farrah et al. (2006) have found evidence for significant clustering in $z = 2$–3 SWIRE starburst-dominated ULIRGs, suggesting that powerful star formation might indeed be taking place preferentially within high density environments. Identifying powerful ULIRGs in the distant Universe is particularly important, not only because they may be the most massive galaxies in the process of formation, but also because they may trace the rarest, most massive dark matter halos at $z \sim 2$ ($M > 10^{13}$ $M_\odot$, density < 10^{-7} Mpc^{-3} at $z = 2$). SWIRE has sufficient volume to include about 85 halos with mass $>10^{14}$ $M_\odot$ in the redshift range $z = 2$–3 (Jenkins et al. 2001; Mo & White 2002), which will evolve to host extremely rich clusters of the Perseus class in the local Universe. For comparison, all the Spitzer deep surveys (extended-GOODS, S-COSMOS, GTO Deep, Dickinson et al. 2003; Sanders et al. 2007; Fazio et al. 2004a) together potentially sample about 9 such haloes. The First Look Survey (FLS, Soifer et al. 2004) and GTO-Bootes survey (Eisenhardt et al. 2004) potentially sample 24 similar haloes, but they are shallower than SWIRE, thus the number of IRAC-selected detectable sources is smaller. Finally, the sub-mm surveys to date have sampled a volume too small to identify even one halo with $M > 10^{14}$ $M_\odot$.

We have therefore selected from SWIRE the brightest mid-IR examples of starburst-dominated ULIRG candidates in the $z = 1.5$–3 range for spectroscopic observation at Keck, to confirm their redshifts and characterize their nature. Our selection of these systems is based on the detection within the Spitzer IRAC bands of the redshifted stellar emission peak at ~1.6 μm in galaxies (Sawicki 2002; Simpson & Eisenhardt 1999). We name these kind of sources "IR-peakers", or "IR-peak sources".

We present here Keck/LRIS multi-object spectroscopy of 35 IR-peak systems in SWIRE northern fields. This instrument provides a nearly contiguous wavelength coverage from the 3000 Å atmospheric cutoff to the Z band ($\lambda_c = 9100$ Å). The UV-optical throughput is larger than 50% in the U to g bands. This represents a great advantage over optical-only spectroscopic surveys: Lyα can be probed to $z \geq 1.7$ and [OII] ($\lambda = 3727$ Å) can be detected at $z \leq 1.4$. Basically, only a very narrow redshift desert exists for IR-peak galaxies observed with LRIS. Moreover, on the 10m Keck telescope, LRIS allows the detection of $r' \simeq 24$ galaxies in reasonably fast exposure times (<2 h).

Several other categories of interesting SWIRE targets have been included in the observations, in order to fill slitlet masks: X-ray, radio, power-law, extremely red, and 24 μm sources.

Section 2 describes the sample selection and the available data in the SWIRE fields; Sect. 3 deals with observations and data reduction. Spectroscopic results are presented in Sect. 4, where we also discuss photometric redshifts. Details on the IR-peak population are given in Sect. 5, including spectroscopy and modeling of broad-band SEDs. Section 6 includes the description of some additional interesting objects: high redshift quasars and X-ray sources. Finally, Sects. 7 and 8 discuss our findings and summarize our conclusions. Throughout this paper we adopt a $H_0 = 71$ [km s^{-1} Mpc^{-1}], $\Omega_{\rm m} = 0.27$, $\Omega_\Lambda = 0.73$ cosmology.

2. Sample selection

The SWIRE Legacy survey (Lonsdale et al. 2003, 2004; Surace et al. 2004) covers 49 deg^2 in all seven Spitzer imaging bands, and has detected over 2 million galaxies up to $z > 3$. This sensitivity means that SWIRE can detect tens of thousands of star-forming galaxies with $SFR \sim$ hundreds $M_\odot$/yr, such as typically found in blank-field submm surveys, in at least two Spitzer bands at $z \sim 1$–3. Such a large ULIRG sample will include not only systems similar to the sub-millimeter galaxy class (SMGs), but also objects dominated by significantly warmer dust than typical of the submm- and mm-selected systems.

2.1. Spitzer data

The SWIRE northern fields benefit from extensive multiwavelength coverage, over the whole electromagnetic spectrum from the X-rays to radio frequencies. The SWIRE datasets are widely described by Surace et al. (2004).

The SWIRE Lockman Hole field is centered at RA = 10h45m00s, Dec = +58d00m00s, with a total area of 10.6 deg^2. Observations with the Infrared Array Camera (IRAC, Fazio et al. 2004b) were obtained in April 2004, and the Multiband Imaging Photometer (MIPS, Rieke et al. 2004) data were collected in May 2004.

The SWIRE ELAIS-N1 field is centered at RA = 16h11m00s, Dec = +55d00m00s, and covers 9 deg^2; Spitzer observations were carried out during January and February 2004.

The SWIRE ELAIS-N2 field is centered at RA = 16h36m48s, Dec = +41d01m45s, over 4 deg^2 and was observed in July 2004.

Data processing is described by Surace et al. (2004) and Shupe et al. (in prep.), and consists of Basic Calibrated Data (BCD) by the SSC pipeline plus post-processing aimed at artifact removal, mosaicking and source extraction. The mosaicking was performed with the SSC routine MOPEX, and source extraction with SExtractor (Bertin & Arnouts 1996). IRAC fluxes were extracted through a 1.9″ diameter aperture and corrected to total fluxes following SSC prescriptions; MIPS fluxes were extracted by means of PRF fitting (see Surace et al., and MIPS Data Handbook 2006). The 5σ depths (consistent with the 90% completeness levels) of the Spitzer data are on average 3.7, 7.4, 43, 46, and 195 μJy at 3.6, 4.5, 5.8, 8.0, and 24 μm, respectively (Surace et al., in prep.), with field to field variations. None of the primary targets is detected at 70 and 160 μm in the SWIRE survey, at the average 5σ flux limits of 17.5 and 112 mJy respectively.

2.2. Available optical data

The Lockman Hole field was observed in the U, g', r', and i' bands with the MOSAIC Camera at the Kitt Peak National Observatory (KPNO) Mayall 4m Telescope, February 2002 (g', r', and i') and January 2004 (U band). The scale of the Camera is 0.26″/pix and the field of view is 36′ × 36′. The astrometric mapping of the optical MOSAIC data is good to less than 0.4″ and the seeing varied between 0.9 and 1.4 arcsec. Data reduction was performed with the Cambridge Astronomical Survey Unit (CASU, Irwin & Lewis 2001) pipeline, following the procedures described in Babbedge (2004). Fluxes were measured within a 3″ aperture (diameter) and corrected to total fluxes using growth curves. Typical 5σ magnitude limits are 24.1, 25.1, 24.4 and 23.7 in U, g', r' and i' respectively (Vega), for point-like sources.

The ELAIS-N1 and EN2 fields were observed in the U, g', r', i' and Z bands, as part of the 2.5m Isaac Newton Telescope (INT, Roque de Los Muchachos, La Palma, Spain) Wide Field Survey (WFS, McMahon et al. 2001). The data were processed with the CASU pipeline; the average limiting magnitudes (Vega, 5σ) across the fields are 23.40 (U), 24.94 (g'), 24.04 (r'), 23.18 (i') and 21.90 (Z). The overall photometric accuracy of the INT WFS survey is 2% Further details are given in Babbedge (2004) and Surace et al. (2004).

2.3. X-ray and radio data

A 0.6 deg^2 sub-area of the Lockman hole field, centered at RA = 10h46m, Dec = 59d01m was observed with the Chandra Advanced CCD Imaging Spectrometer (ACIS-I, Weisskopf et al. 1996) in the X-rays, during September 2004. Description of observations and data analysis is provided in Polletta et al. (2006). The total exposure time was 70 ks, reaching 3σ fluxes of $\sim 10^{-15}$, 5×10^{-16}, and 10^{-14} [erg cm^{-2} s^{-1}] in the broad (0.3−8 keV), soft (0.3−2.5 keV) and hard (2.5−8 keV) bands respectively.

As part of the ELAIS Deep X-ray Survey (EDXS), a sub-region of ELAIS-N1 was targeted by the Chandra ACIS instrument. Observations and data analysis are described in Manners et al. (2003, 2004) and Franceschini et al. (2005). The Chandra field is centered at RA = 16h10m20.11s, Dec = +54d33m22.3s (J2000.0) and the total net exposure time is 71.5 ks (after flare cleaning). Sources were detected to flux levels of 2.3×10^{-15}, 9.4×10^{-16} and 5.2×10^{-15} [erg cm^{-2} s^{-1}] in the 0.5−8 keV, 0.5−2 keV and 2−8 keV bands.

Finally, a deep, 1.4 GHz radio survey, centered at RA = 10h46m, Dec = 59d01m covers 40′×40′ in the Chandra/SWIRE Lockman Hole field. These data were obtained in multiple Very Large Array (VLA) runs, obtained in Dec. 2001, Jan.–Mar. 2002, and Jan. 2003 (Owen et al., in prep.) with configurations A/B/C and D. The total integration time spent on source is 500 ks. The rms noise at the image center is 2.7 μJy (see also Polletta et al. 2006).

2.4. Primary targets

Primary targets were selected in order to include SWIRE $z > 1.5$ ULIRG candidates. The near-IR restframe spectral energy distribution (SED) of galaxies is characterized by a peak at 1.6 μm, due to the Planck spectrum of low-mass stars (dominated by M-type), enhanced by a minimum in the H$^-$ opacity in stellar atmospheres (Sawicki 2002). On the red side of the peak, molecular absorption bands further blue the (H–K) color. This peak is fully characterized by the IRAC instrument if at least one of the IRAC photometric bands (3.6, 4.5, 5.8, 8.0 μm) falls long- or shortward of the peak. This happens when the peak lies in the 4.5 or 5.8 μm band, i.e. for redshifts in the range z = 1.4–3.0.

IRAC was in part designed for photometric selection of galaxies at these redshifts displaying this feature (Simpson & Eisenhardt 1999). Egami et al. (2004) have shown that starburst-dominated SMGs show this stellar population features strongly in the IRAC SEDs.

We have selected "IR-peak" sources by exploiting SWIRE Spitzer photometry, isolating objects with SEDs peaking at 4.5 or 5.8 μm, in the SWIRE Lockman Hole, ELAIS-N1 and N2 fields. The density on the sky of these sources is about 200 deg^{-2}, at the SWIRE flux limits (Lonsdale et al., Berta et al., in prep.).

All sources are detected in the 3.6, 4.5 and 5.8 μm bands; for some only an upper limit to the 8.0 μm flux is available (see Table 2). In the latter case, this upper limit is required to be consistent with the IR-peak definition, i.e. lower than the 5.8 μm measured flux.

Optical magnitudes were limited to the $r' < 24.5$ (Vega) range, in order to include sources bright enough to be detected with LRIS. Moreover objects brighter than $r' < 21$ were avoided, in order to minimize the contamination by low redshift foreground sources (see Fig. 1).

On average, 4 IR-peak galaxies were put onto a slit per LRIS mask (see Table 1). Table 2 reports the basic data for the selected IR-peak targets. The total number of IR-peakers observed is 35.

2.5. Mask fillers

LRIS masks can host as much as 30 slitlets, the exact number depending on the positions of the selected targets on the sky.

In addition to the primary IR-peakers included in each mask, the remaining slitlets were filled with sources from the SWIRE catalogs showing interesting photometric multi-wavelength properties, such as red optical-NIR colors ($[i-4.5] \geq 5$), consistent with $z \sim 1$ systems, X-ray or radio detection, IRAC red power-law (AGN-like) with a monotonic slope, and finally generic 24 μm detection.

Column eight in Tables 5 and 6 reports a rough classification of the most interesting sources, based on their photometric properties. In particular, we distinguish: 4.5 μm- and 5.8 μm-peak galaxies (P2, P3, P3L[2]), X-ray and radio sources (X and R in Col. 8), and objects with a monotonic power-law like IRAC SED (pow).

The total number of mask is 4 in the Lockman Hole field, which have been observed during the first three hours of each night, three in ELAIS-N1 and three in ELAIS-N2. A total of 235 slits were defined. Figure 1 shows all targets detected in the mid-IR, in the r'-band vs. 24 μm space.

These masks include 35 IR-peak targets (9 4.5 μm and 26 5.8 μm peakers), 7 X-ray sources, 12 radio sources, 19 IRAC power-law objects and 139 objects detected in the MIPS 24 μm channel. Figure 2 shows the distribution of the selected targets in the IRAC color-space (Lacy et al. 2004; Stern et al. 2005); different symbols refer to different photometric (and spectroscopic) properties: IR-peak sources (filled circles), power-law IRAC SEDs (crosses), broad-line objects (open squares). It is already worth noting that the power-law and broad-line classifications are $\sim$100% consistent with each other, these targets lying in the locus of AGNs in the IRAC color space (Lacy et al., see also Sect. 5).

3. Observations and data reduction

Observations were carried out in multi-object mode with the Low Resolution Imaging Spectrometer (LRIS, Oke et al. 1995) at the Cassegrain focus of the Keck-I telescope, during the nights of May 27th and 28th, 2006.

The LRIS instrument makes use of a dichroic to split the incoming light into a blue and red beam. Gratings, grisms and filters can be changed independently for the two beams. We have adopted the dichroic designed to split light at 5600 Å.

As far as the blue arm is concerned, in order to obtain a maximum throughput in the spectral range 3200–5000 Å, we used the 400 lines/mm grism, blazed at 3400 Å, providing a good throughput from the atmospheric cutoff at 3000 Å to the dichroic 5600 Å limit.

On the red arm, we used the 400/8500 grating, blazed at 7400 Å, providing wavelength coverage up to ~9550 Å. This configuration was chosen in order to optimize spectral coverage of simultaneous LRIS red and blue observations, as well as wavelength calibration with Hg, Cd, Zn, Ar arc lamps. The effective spectral coverage depends on the positioning of slitlets in the mask, relative to the telescope focal plane.

The dispersion in the blue and red arms is 1.09 Å/pix and 1.86 Å/pix. A 1.2 arcsec slit was adopted, resulting in an instrumental resolution (measured as the *FWHM* of arc lines) of $\sim$10.5 Å. This corresponds to 750 and 420 [km s^{-1}] at 4200 and 7500 Å, respectively. The seeing varied between $\sim$1.0 and $\sim$1.3 during the two observing nights.

The slit masks cover an effective area of 6×8 arcmin^2 on the sky; between 15 and 30 slitlets with variable length were placed per mask, this number depending on the sky distribution of the selected targets. A total of 10 masks was observed during the two night run, with exposure times between 3600 s and 5400 s, split into three exposures per mask. Table 1 lists the position of the pointings on the sky, as well as exposure times, number of slitlets and number of IR-peak targets included.

Spectro-photometric standard stars Feige34 and BD+28D4211 were observed during the nights, taking care to have as close an airmass as possible to the science pointings. Flat field and arc lamp frames were taken at the same telescope position (ALT,AZ) as the science spectra, in order to reproduce the same instrumental flexures and shifts and avoid troublesome corrections during data reduction. Arc-frames were obtained using Hg, Cd, Zn, Ar lamps, ensuring bright calibration lines over the whole spectral range from 3000 Å to 9500 Å, with a gap between 5500 and 6500 Å only.

Data reduction was carried out by using the standard tasks in the IRAF[3] environment. Bias, dark and flat field corrections were performed in the standard manner, by using the overscan CCD regions and the dome flat field frames obtained at the telescope, as well as the gain values reported on the LRIS webpage[4] for the different amplifiers. Wavelength and flux calibration were performed on the two-dimensional spectra, after background subtraction.

Extraction of spectra was performed in all cases where a continuum trace was detected; lines were identified on non-flux-calibrated frames, in order to avoid losses of spectral coverage due to the relative position of slits with respect to the standard star spectrum. Line properties were measured after flux calibration.

The lines detected for the IR-peak galaxies are listed in Tables 3 and 4, where we list observed wavelengths, equivalent widths, FWHMs (corrected in quadrature for the instrumental resolution) and derived redshifts.

Spectroscopic redshifts of all the observed targets are listed in Tables 5 and 6, where we include also the number of emission/absorption lines detected for each object.

4. Results

The full sample of targeted sources includes 233 objects[5], distributed in the Lockman Hole, ELAIS-N1 and ELAIS-N2 SWIRE fields.

We have computed redshifts on the basis of the presence of emission lines, both in the ultraviolet and optical restframe domains, such as Lyman-α (λ = 1216 Å), NIV (λ = 1240 Å), OI (λ = 1304 Å), SiIV, OIV] (λ = 1400 Å), NIV] (λ = 1486 Å), CIV ($\lambda\lambda$ = 1548, 1551 Å), HeII (λ = 1640 Å), CIII] (λ = 1909 Å), MgII ($\lambda\lambda$ = 2796, 2803 Å), FeII and FeIII lines (λ = 2000–3000 Å), [OII] ($\lambda\lambda$ = 3726, 3729 Å), as well as Balmer Hydrogen emission and absorption, CaII-HK, [OIII], [NII], and [SII] lines for lower redshift sources. We do not have adequate resolution to resolve the [OII], CIV and MgII doublets.

The spectroscopic success rate per mask strongly depends on the observing conditions, such as presence of cirrus, seeing and airmass. The last column in Table 1 lists the number of

[2] P3L sources have IRAC 3.6, 4.5, 5.8 μm detection, but only an upper limit at 8.0 μm.

[3] The package IRAF is distributed by the National Optical Astronomy Observatory which is operated by the Association of Universities for Research in Astronomy, Inc., under cooperative agreement with the National Science Foundation.

[4] http://www2.keck.hawaii.edu/inst/lris/

[5] Note that a couple of targets were observed twice, in distinct masks, therefore the effective number of targets is 233 in 235 slitlets.

Table 1. Summary of observations: each mask is named with the identification number of its primary target. The number of slitlets, of IR-peakers included, and of measured spectroscopic redshifts are reported.

Mask	RA J2006.4	Dec J2006.4	PA [deg]	AM	t(exp) [s]	N (slits)	N (peak)	N (reds*)
LH_247597	10:52:32.694	+57:46:27.896	110	1.55	3600	21	5	6
LH_575325	10:47:43.555	+59:09:22.974	131	1.35	4500	26	5	15
EN1_205467	16:09:42.168	+54:39:49.085	155	1.25	3600	24	3	18
EN1_282078	16:16:56.673	+55:32:02.568	179	1.26	5400	24	2	18
EN2_273717	16:33:33.569	+40:54:40.722	143	1.21	5400	23	3	15
LH_128777	10:59:03.752	+57:46:56.282	105	1.56	3600	29	3	11
LH_579894	10:48:09.714	+59:09:25.529	119	1.36	4500	24	6	9
EN1_341469	16:03:38.599	+54:23:52.565	180	1.23	5400	24	4	16
EN2_10334	16:42:09.003	+40:45:51.746	104	1.22	5400	25	2	20
EN2_172324	16:34:50.206	+41:00:10.745	145	1.08	4500	15	4	11

* Without accounting for serendipitous sources.

Table 2. Data for IR-peak sources included in slit, sorted by field: basic photometric information, photometric flag, spectroscopic classification and redshift are listed. See Table 5 for more details on flags.

ID #	RA [J2000]	Dec [J2000]	r mag [Vega]	S(3.6) [μJy]	S(4.5) [μJy]	S(5.8) [μJy]	S(8.0) [μJy]	S(24) [μJy]	flag	Class spec	z spec	z phot
EN1_202261	242.330640	54.676624	23.80	64.67	69.01	51.93	48.58	215.08	P2	ELG	1.339	1.190
EN1_205467	242.429490	54.697529	23.40	36.37	55.60	83.10	70.62	488.24	P3,X,pow	–	–	0.370
EN1_202260	242.401140	54.636532	22.51	41.17	51.12	39.44	70.48	287.73	P2,X	BLAGN	1.545	1.480
EN1_282078	244.260240	55.522625	21.81	38.14	50.96	60.11	51.37	319.00	P3	BLAGN	1.685	1.770
EN1_279954	244.184220	55.511967	22.49	31.88	42.02	59.95	58.22	357.72	P3,pow	BLAGN	2.409	2.770
EN1_341469	240.850890	54.447605	24.07	103.34	119.90	120.89	78.24	992.89	P3	–	–	1.540
EN1_342445	240.908420	54.440781	23.94	27.47	31.50	44.91	–	213.89	P3L	ELG	1.917	1.850
EN1_340451	240.826570	54.434467	23.32	38.87	54.19	63.95	58.84	181.78	P3	NLAGN	2.866	2.320
EN1_339960	240.867170	54.399624	23.75	50.34	62.56	62.94	60.88	248.89	P3	BLAGN	1.475	1.590
EN2_275226	248.302110	40.966358	23.74	38.23	53.61	–	45.04	386.97	P2	BLAGN	1.710	1.670
EN2_273717	248.339860	40.951962	22.66	66.07	72.91	89.64	81.37	1121.32	P3	BLAGN	1.800	3.050
EN2_269695	248.418080	40.900318	23.17	42.83	48.45	57.50	50.11	768.10	P3	–	–	1.800
EN2_10334	250.438280	40.763359	23.86	81.45	92.74	96.24	73.20	1073.62	P3	–	–	2.010
EN2_11091	250.464570	40.791348	23.51	49.68	50.87	66.54	–	358.14	P3L	ELG	1.946	2.140
EN2_172324	248.621380	41.059731	22.81	90.04	110.75	151.30	96.05	574.98	P3	NLAGN	1.739	2.070
EN2_167372	248.650680	40.979759	23.40	49.03	50.04	–	–	–	P2L	ELG	1.445	2.120
EN2_166134	248.678600	40.968796	22.87	67.08	68.06	44.93	–	216.85	P2	ELG	1.337	1.470
EN2_165986	248.712040	40.980968	22.66	27.82	36.04	63.45	58.34	283.55	P3,pow	BLAGN	2.163	0.430
LH_247598	163.005920	57.852535	23.41	39.59	42.56	43.17	–	241.24	P3L	–	–	1.130
LH_245973	163.022840	57.795551	23.09	25.37	36.08	47.37	–	605.48	P3L	–	–	2.840
LH_247451	163.070590	57.811264	23.42	50.56	61.40	75.27	59.32	351.28	P3	–	–	1.790
LH_245782	163.066380	57.765423	23.49	39.83	45.38	32.88	–	–	P2	–	–	1.590
LH_247597	163.096080	57.802212	23.24	51.16	60.40	76.15	51.76	871.90	P3	–	–	1.780
LH_571442	161.700320	59.199207	24.31	21.28	30.67	35.41	33.76	–	P3	–	–	3.210
LH_572243	161.780960	59.178944	22.94	25.94	30.26	28.69	–	231.34	P2,X	NLAGN	1.820	1.840
LH_575068	161.886430	59.201855	24.44	30.45	34.50	40.03	–	299.99	P3L,R	–	–	1.690
LH_572257	161.848860	59.143932	22.91	24.85	33.69	34.50	31.46	229.24	P3,X	SB	0.249	2.170
LH_574364	161.909820	59.169308	23.46	44.36	50.97	52.29	47.69	722.57	P3,R	NLAGN	1.474	1.550
LH_125952	164.566760	57.835228	24.46	34.68	38.04	46.91	–	–	P3L	–	–	2.140
LH_126546	164.669680	57.792194	23.18	36.65	46.40	57.55	–	501.02	P3L	–	–	1.920
LH_128777	164.722290	57.832966	24.37	54.40	71.86	105.16	64.84	819.83	P3	–	–	2.140
LH_577220	161.935620	59.236961	23.69	27.75	34.55	41.80	–	522.93	P3L,R	–	–	2.420
LH_576281	161.935760	59.210655	23.99	35.83	44.53	39.46	35.84	416.95	P2	–	–	1.780
LH_574939	161.917590	59.181812	23.47	45.26	50.26	54.08	–	300.18	P3L	–	–	1.810
LH_577291	162.032840	59.188950	23.81	40.68	49.33	64.18	38.59	407.16	P3	–	–	1.800

redshifts obtained for each mask, without accounting for serendipitous sources.

Lockman Hole masks were observed during the first hours of each night, at increasing airmass, with relatively poor results (see Table 1). During the first night, 6/21 and 15/26 sources have a successful redshift estimate for masks LH_247597 and LH_575325 respectively[6]. Masks LH_128777 and LH_579894, observed on the second night, turn out to have 11/29 and 9/24 good spectroscopic redshifts, without taking into account serendipitous sources.

[6] These numbers don't include serendipitous sources.

It is worth to note that mask LH_579894 has a success rate as low as LH_128777 (~38%), despite the lower airmass (1.36 vs. 1.56). The main reason for this effect is that the former contains fewer 24 μm-bright targets than the latter (45% vs. 60% of the objects in slit), resulting in a lower emission lines detection rate.

The ELAIS fields were observed at lower airmasses, hence the success rate is higher for these areas, being 73% on average, with a 80% peak in the best case. A total of 139 redshifts have been derived for the targeted objects.

The redshift uncertainty depends on the number of detected spectral features. In the case that only one emission line is detected, the sources of uncertainty on the redshift estimate are

Table 3. Detected lines for IR-peak targets, sorted by mask (first night). For each source, we report the observed wavelength, equivalent width (EW), full width at half maximum (FWHM, corrected for the instrumental resolution) and identification of the detected spectral features. For each detected line, the spectroscopic redshift is computed (last column).

ID	Cont. λ range [Å]		Detected lines				z
SWIRE	blue	red	λ [Å]	*EW* [Å]	*FWHM* [Å]	line	
LH_247598	3500–5000	8800–7800	–	–	–	–	–
LH_245973	–	6000–8500	–	–	–	–	–
LH_247451	4000–5000	5500–8300	–	–	–	–	–
LH_245782	4400–5500	6500–8000	–	–	–	–	–
LH_247597	3700–5300	5500–8000	–	–	–	–	–
LH_571442	–	7100–9000	–	–	–	–	–
LH_572243	3300–5000	6100–8500	3422.6	–116.2	<10.50	Lyα(1216)	1.815
			4374.5	–36.3	11.20	CIV](1549)	1.824
			5383.4	–	12.49	CIII](1909)	1.820
LH_575068	3500–4300	5600–8200	–	–	–	–	–
LH_572257	3300–5600	6200–8700	4650.1	–63.3	<10.50	[OII](3727)	0.248
			6255.9	–38.0	<10.50	[OIII](5007)	0.249
			8193.4	–60.18	<10.50	Hα(6563)	0.248
LH_574364	3400–5000	5700–8300	6922.8	–114.0	8.78	MgII(2800)	1.474
EN1_202261	–	6200–9000	8717.0	–39.3	<10.50	[OII](3727)	1.339
EN1_205467	3500–5300	5600–8300	–	–	–	–	–
EN1_202260	3000–5600	5700–9500	3942.5	–449.8	60.61	CIV(1549)	1.545
			4169.3	–22.2	21.62	HeII(1640)	1.541
			4845.6	–111.8	74.07	CIII]1909	1.538
			7119.7	–380.5	154.24	MgII(2800)	1.545
EN1_282078	3100–5200	5500–8200	3262.3	–23.7	48.58	Lyα(1216)	1.683
			3762.9	–62.7	98.73	SiIV,OIV](1400)	1.688
			4152.4	–118.9	79.41	CIV(1549)	1.681
			5673.6	–188.7	239.87	FeII	–
			7517.2	–132.7	133.29	MgII(2800)	1.687
EN1_279954	3200–5600	5700–8500	4176.6	–242.3	143.82	Lyα(1216)	2.435
			4157.7	–5.7	<10.50	Lyα(1216)	2.419
			4173.9	–10.8	<10.50	Lyα(1216)	2.432
			4778.3	–94.8	108.90	SiIV,OIV](1400)	2.413
			5280.7	–94.9	68.99	CIV(1549)	2.409
			5947.2	–98.7	166.47	NIII](1750)	2.398
			6512.7	–198.2	118.23	CIII](1909)	2.412
EN2_275226	3300–5700	5600–8500	3377.6	–143.3	17.29	NV(1240)	1.724
			4211.7	–294.3	96.77	CIV(1549)	1.719
			5153.7	–227.8	130.78	CIII](1909)	1.700
			7544.8	–126.9	112.71	MgII(2800)	1.697
EN2_273717	3300–5600	5600–8600	3478.8	–129	>100	NV(1240)	1.806
			3949.7	–64	83.54	SiIV,OIV](1400)	1.821
			4325.4	<–38.0	48.37	CIV(1549)	1.792
			5347.8	–52.1	98.64	CIII](1909)	1.801
EN2_269695	3200–5100	5600–8100	–	–	–	–	–

given by the wavelength calibration of the spectrum (having a typical rms of 0.7–1.0 Å) and the centroid uncertainty in positioning during the Gaussian fit to the line profile (which is a fraction of a pixel and negligible with respect to estimating redshifts). When dealing with multiple line detections, the average z is computed and the uncertainty is given by the dispersion of the average. Typical uncertainties on z are thus smaller than $\Delta z = 0.01$ for narrow lines. In the case of broad emission lines, a lorentzian fit to the lines was usually adopted, but the asymmetry and broadness of profiles cause the uncertainty of line positioning to be larger and dominate the Δz. In this case, the redshift uncertainty can be as large as $\Delta z = 0.03$.

In addition to the formally targeted objects, 68 serendipitous sources were detected, and for 35 of these a redshift estimation was possible. We have identified these serendipitous objects by measuring their projected distance from the main target in the same slit, matching it to the SWIRE multi-wavelength catalog, and visually seeking for SWIRE counterparts on r' band and 3.6 μm images. Only 15 were identified, while another 14 are detected in the optical but not by Spitzer. Among these, only 11 have a spectroscopic redshift. In Tables 5 and 6 we list only those serendipitous sources with a SWIRE/Spitzer counterpart.

The total number of redshifts available is 174, for a total of 301 objects in slits; 150 sources with redshift have a SWIRE identification.

4.1. Photometric redshifts

Taking advantage of the extensive multiwavelength coverage available in the observed areas, we have computed photometric redshifts for all the targeted sources, by using the Hyper-z (Bolzonella et al. 2000) and the Rowan-Robinson (2003) codes.

In the former case, we have adopted a semi-empirical template library including GRASIL (Silva et al. 1998) models of spiral and elliptical galaxies, M 82 and Arp220 templates (Silva et al.) upgraded with observed PAH mid-IR features, a ULIRG template (IRAS 19254-7245, Berta et al. 2003), type-1 AGN and Seyfert templates by Polletta et al. (in prep.), obtained by averaging observed AGN SEDs. The fits were performed using only the optical and IRAC (3.6–8 μm) data, ignoring the MIPS 24 μm flux. Tests including the 24 μm data have been attempted as well, but they have shown a higher degree of degeneracy and aliases in the photometric redshift estimate.

Table 4. Detected lines for IR-peak targets, sorted by mask (second night).

ID	Cont. λ range [Å]		Detected lines				z
SWIRE	blue	red	λ [Å]	*EW* [Å]	*FWHM* [Å]	line	
LH_125952	–	–	–	–	–	–	–
LH_126546	3500–5600	6000–8300	–	–	–	–	–
LH_128777	–	–	–	–	–	–	–
LH_575068	–	–	–	–	–	–	–
LH_577220	–	5600–7600	–	–	–	–	–
LH_576281	3500–5600	5600–8600	–	–	–	–	–
LH_574939	3400–5000	–	–	–	–	–	–
LH_574364	–	6000–8500	6521.87	–39.66	<10.50	Fe	–
			6923.38	–100.2	10.95	MgII(2800)	1.474
			9209.20	–125.6	7.34	[OII](3727)	1.471
LH_577291	–	5700–7500	–	–	–	–	–
EN1_341469	–	5700–8500	–	–	–	–	–
EN1_342445	3300–5500	5600–8500	3545.82	–177	6.31	Lyα(1216)	1.916
			4518.67	–47.75	13.76	CIV(1549)	1.917
EN1_340451	–	–	4702.81	–141.7	8.92	Lyα(1216)	2.867
			6343.29	–21.04	14.87	HeII(1640)	2.868
			7373.11	–	–	CIII](1909)	2.862
EN1_339960	3600–5600	5700–8500	3834.78	–101.9	27.66	CIV(1549)	1.476
			4720.29	–47.48	28.67	CIII](1909)	1.473
EN2_10334	4000–5600	6000–8500	–	–	–	–	–
EN2_11091	4000–5600	5700–8200	3581.76	<60	5.75	Lyα(1216)	1.946
EN2_172324	3100–5700	5700–8500	3333.35	–68.92	7.36	Lyα(1216)	1.741
			4250.45	–41.41	25.17	CIV](1549)	1.744
			4484.25	–24.33	45.54	HeII(1640)	1.734
			5223.39	–21.81	21.37	CIII](1909)	1.736
EN2_167372	3200–5600	6000–9200	9112.03	–35.71	19.06	[OII](3727)	1.445
EN2_166134	3200–5700	5700–9000	8711.26	–31.09	10.23	[OII](3727)	1.337
EN2_165986	3200–5700	5600–8700	3845.90	–	<10.50	Lyα(1216)	2.163
			3872.52	–499.2	146.83	Lyα(1216)	2.185
			4433.21	–51.1	119.74	SiIV,OIV](1400)	2.167
			4897.26	–193.6	118.24	CIV(1549)	2.162
			6026.88	–240.6	225.46	CIII](1909)	2.157

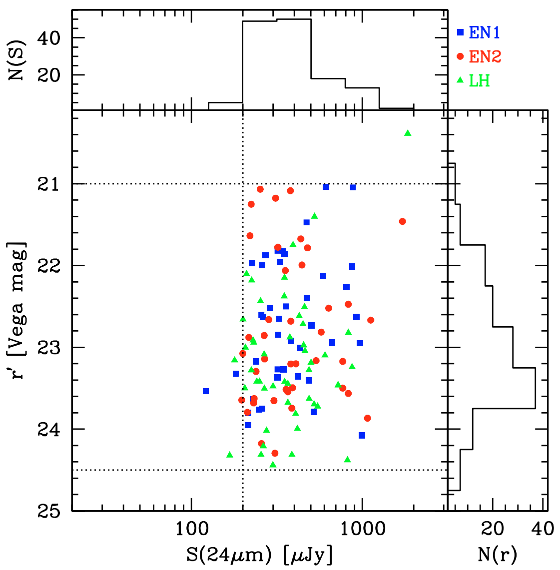

Fig. 1. Selection of sources for our spectroscopic Keck observations: distribution of observed targets in the 24 μm vs. r' space.

The photometric redshifts thus obtained are compared to the spectroscopic Keck results in Fig. 4 (left panel). The dashed and dotted lines represent 10% and 20% uncertainty, respectively. Filled circles represent IR-peak sources, crosses are objects with power-law IRAC SEDs, and open squares indicate broad-line detections. All other cases are plotted as open circles.

Outliers are mostly AGNs (crosses or open squares in Fig. 4), typically showing a power-law spectral energy distribution from the optical to the mid-IR. In this kind of object, neither strong, nor sharp features are detected in the broad band SEDs, therefore the photometric redshift estimate often fails.

Accounting for all sources with a spectroscopic redshift, the r.m.s. of the distribution[7] of $\Delta(1+z)$ is 0.095. Excluding power-law sources, it decreases to 0.069. The semi inter-quartile range (s.i.q.r.) computed for all sources is 0.028.

The results obtained by using the Rowan-Robinson (2003) code are shown in the right panel of Fig. 4. As far as AGN-dominated objects are concerned, the results of this code show a much better consistency between photometric and spectroscopic redshifts for high-redshift sources, while it seems to fail for low-redshift ones. For the latter, the photometric redshift is overestimated. The adopted templates are those described in Rowan-Robinson et al. (2004), including AGN SEDs built on actual ELAIS data. The overall concordance of the photometric estimate and the spectroscopic measure of redshifts is similar to the one obtained with Hyper-*z*, having a $\Delta(1+z)$ rms. and s.i.q.r. of 0.091 and 0.043. The number of dramatic failures (outliers) is smaller than in the Hyper-*z* case, but the median scatter is slightly larger.

Finally, Fig. 3 reports the redshift distribution of our targets with spectroscopic redshift. The white histogram represents the distribution of spectroscopic redshifts for all sources, while the shaded histogram includes only IR-peak objects.

[7] Here Δ is the difference between the photometric and spectroscopic redshift estimates.

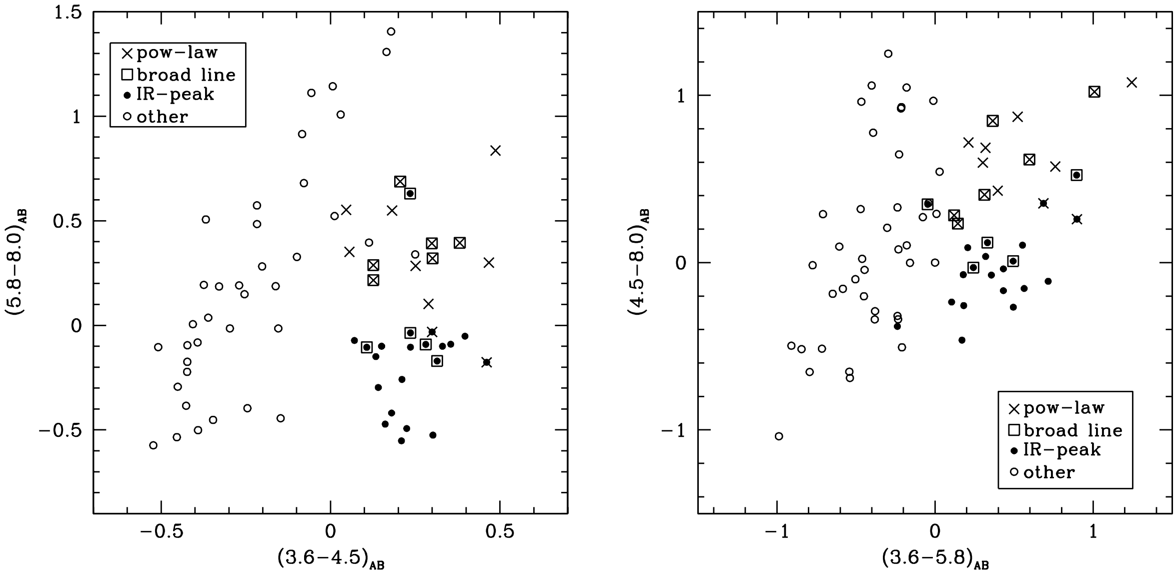

Fig. 2. Distribution of the observed targets in IRAC color space (Stern et al. 2005; Lacy et al. 2004). We distinguish: IR-peak sources (filled circles), power-law targets (crosses), broad-line detections (open squares). All other cases are plotted as open circles.

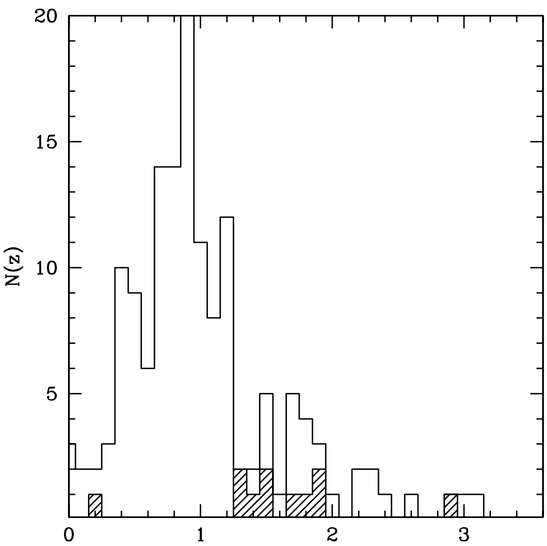

Fig. 3. Redshift distribution of successfully detected sources (spectroscopic z). The empty histogram shows spectroscopic redshifts for all sources, while the shaded histogram represents IR-peak sources alone.

4.2. Spectroscopic classification

The last column in Tables 5 and 6 reports the spectral classification of targets, based on the detected lines. We classify as simply "emission line" galaxies (ELG), those sources with insufficient lines to apply any diagnostic technique, i.e. sources with only one or two lines detected. Similarly, "absorption line" galaxies (ALG) have only absorption lines detected.

When possible, emission line fluxes were corrected for extinction, as derived from the observed Balmer decrement (using the available Balmer lines and assuming case-B recombination, Hummer & Storey 1987).

We classify starburst galaxies (SB) on the basis of different criteria:

- presence of strong emission lines (e.g. [OII], λ = 3727 Å) and young star absorption lines (e.g. type-A stars), such as the advanced Balmer series, from Hδ down to H-10;
- conformity to optical diagnostic diagrams for AGN/starbursts, based on optical emission lines (Veilleux & Osterbrock 1987; Dessauges-Zavadsky et al. 2000; Baldwin et al. 1981);

Type-1 AGNs (BLAGN flag) are recognized through the presence of broad emission lines ($FWHM$ > 1000 [km s^{-1}]), both in the ultraviolet and optical restframe spectral domains.

Type-2 AGNs (NLAGN) are identified by the presence of high-ionization narrow emission lines (e.g NV, CIV, HeII, [NeV], λ = 1240, 1549, 1640, 3426 Å) in the observed spectra (e.g. Farrah et al. 2005; Villar-Martin et al. 1996; Allen et al. 1998), or on the basis of optical diagnostic diagrams (e.g. Veilleux & Osterbrock 1987; Baldwin et al. 1981) in some cases. Because only a few optical emission lines are available, a distinction between Seyfert-2 galaxies and LINERs is not possible, apart in one case (EN1_340460, at the boundary between starbursts and LINERs). It is worth specifying that ultraviolet emission lines such as CIV can be produced also by star forming activity, typically being heated by O stars, but are always associated with a P-Cyg profile, produced by stellar winds with velocities higher than 1000 [km s^{-1}] (e.g. Shapley et al. 2003; Farrah et al. 2005). Given the resolution of our spectra, when no P-Cyg profile is detected and the CIV (λ1549 Å) line is observed as narrow emission only, a type-2 AGN explanation is favored.

Globally, 122 narrow-line emission galaxies have been classified. Among these, 44 have enough spectroscopic information to allow a unambiguous classification: 39 turn out to be starbursts and 5 type-2 AGNs, at least in the sampled optical range. Seven galaxies show only absorption lines (typically the CaII-HK doublet and some advanced Balmer Hydrogen lines), and 17 are type-1 AGNs. Finally, four stars were identified in our slitlets.

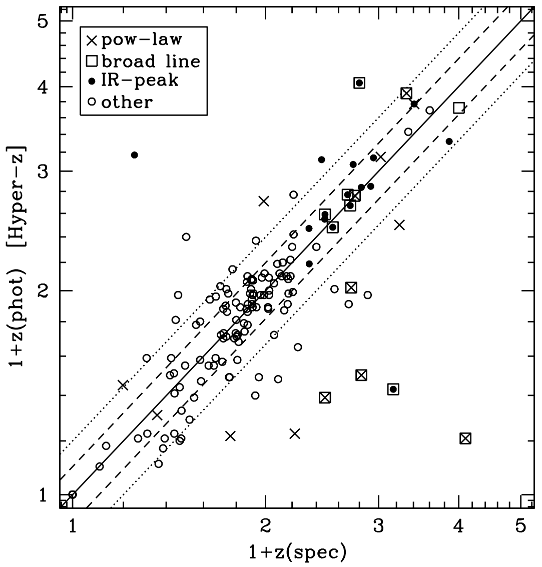

Fig. 4. Comparison between spectroscopic and photometric redshifts. Dashed and dotted lines represent ±10 and 20% uncertainties. *Left panel*: results obtained with Hyper-z (Bolzonella et al. 2000). *Right panel*: results of the Rowan-Robinson (2003) code.

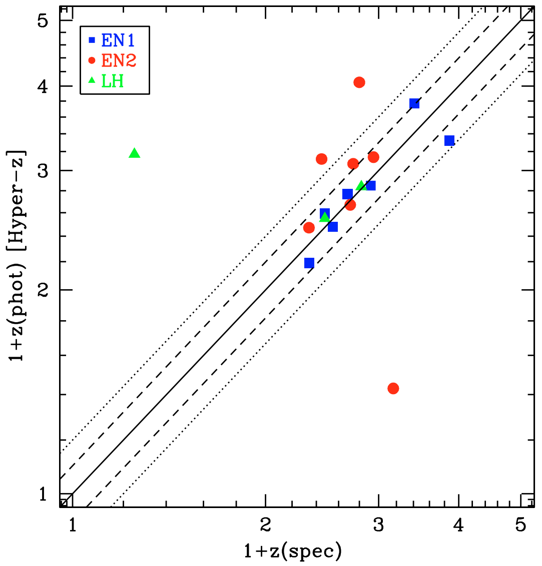

Fig. 5. Comparison between spectroscopic and photometric redshifts for IR-peak sources. *Left panel*: results obtained with Hyper-z (Bolzonella et al. 2000). *Right panel*: results of the Rowan-Robinson (2003) code.

5. IR-peak galaxies

As far as IR-peak sources are concerned, a total of 35 targets were included in our 10 masks; among these, 11 galaxies have a confirmed spectroscopic redshift in the range z = 1.5–3.0, 5 lie between $1.0 < z < 1.5$, and one turned out to be a low redshift ($z < 1.0$) (confused, see below) interloper. For the remaining 18 IR-peak targets no spectral features were detected, but in all cases a non negligible continuum is present (Cols. 2–3 in Tables 3 and 4 specify if a continuum was detected in the blue and/or red LRIS arms and over which wavelength range).

Figure 7 shows the spectra and SEDs of IR-peak targets with spectroscopic redshifts, the distinction between 4.5 μm- and 5.8 μm-peak being obvious.

Tables 3 and 4 list the basic measured properties of the detected lines for IR-peak galaxies, including the equivalent width (EW), full width at half maximum (FWHM, corrected for the instrumental resolution), observed wavelength and identification. In the last columns of Table 2, spectroscopic and photometric redshifts for these targets are listed.

Infrared peakers lie in the fourth quadrant of the IRAC color space ([3.6–5.8] > 0, [4.5–8.0] < 0 in the right panel of Fig. 2; or [3.6–4.5] > 0, [5.8–8.0] < 0 in the left panel). Objects at the boundary between the IR-peak and AGN-torus loci (i.e. [4.5–8.0] ≃ 0.0, [3.6–5.8] > 0) display mixed properties. For example, found here are objects showing a power-law like IRAC SED, with a smooth 5.8 μm-peak superimposed (filled circles with crosses). These can be interpreted as a 5.8 μm peak diluted by AGN-torus power-law emission. Other composite galaxies show a clear IRAC peak shape, but their restframe UV spectra are dominated by broad-line emission (filled circles within open

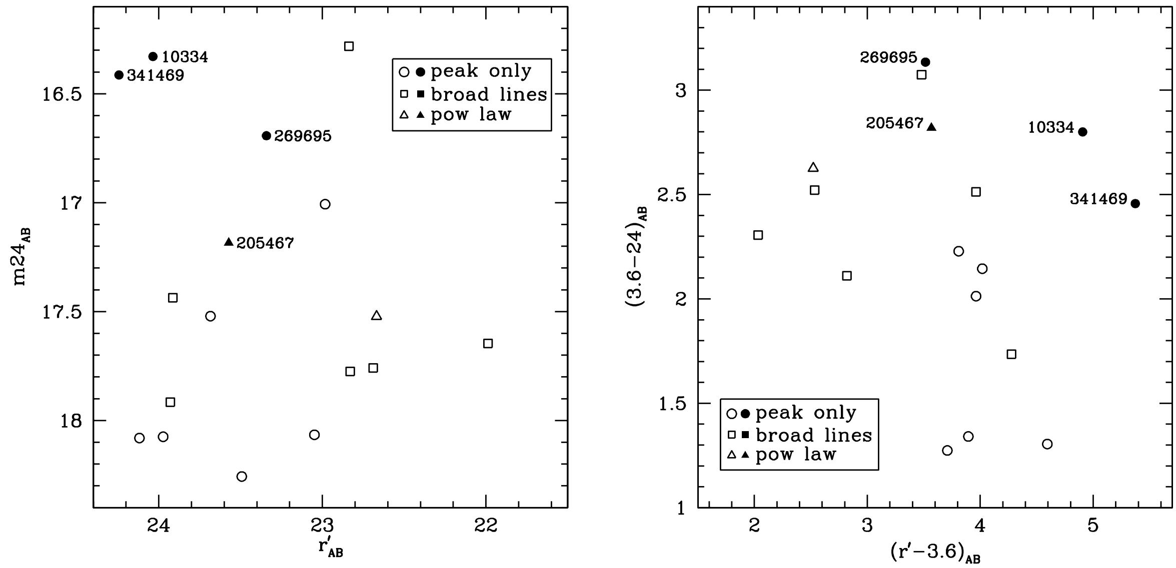

Fig. 6. Distribution of IR-peak targets in the optical-IR color space (ELAIS-N1 and N2 only). Open symbols belong to sources with a spectroscopic redshift, filled ones represent objects with no spectral features detected.

squares). The properties of individual IR-peakers are discussed below.

Figure 5 presents the comparison between spectroscopic and photometric redshifts for IR-peakers only, obtained with the Bolzonella et al. (2000) (left hand side) and Rowan-Robinson (2003) (right) codes. The two principal outliers (in the Hyper-z case) are a Lockman Hole source with spectroscopic redshift of $z = 0.249$, which turns out to be a confused object (see below) and a broad-line object in ELAIS-N2. In the latter case, the Hyper-z code could not find a reliable redshift by adopting a QSO template, because of the almost featureless continuum, and then it completely underestimated the photometric z. The Rowan-Robinson et al. (2004) templates seem to solve these troubles, but underestimate the redshift of a 4.5 μm-peaker in ELAIS-N1 (EN1_202261) with a very red $r' - Z$ color (see Fig. 7), which probably was interpreted as a deep Balmer break at $z < 1$.

5.1. 4.5 μm-peak sources

Eight 4.5 μm-peak galaxies were observed. Three of these sources have a confirmed spectroscopic redshift between $z = 1.30$ and $z = 1.45$, with narrow emission lines (EN1_202261, EN2_167372, EN2_166134). The detected features are not enough to distinguish between starburst or AGN activity (see Sect. 4.2), therefore we put these sources in the general "ELG" class. For two of these targets the photometric redshifts agree with the measured spectroscopic values (see Table 2), while for source EN2_167372 the two are not consistent with each other ($z_{\rm phot} = 2.120$, $z_{\rm spec} = 1.445$). For this source, IRAC photometry is available only in channels 1 and 2, while both the 5.8 and 8.0 μm bands have only an upper limit. It is possible that the photometric estimate of redshift has been affected by the lack of near-IR restframe data.

A fourth 4.5 μm-peak object lies at $z = 1.545$ (target EN1_202260) and is characterized by broad emission lines, which testify to the presence of a type-1 AGN component contributing to the UV-optical emission. This object is detected also in the X-rays. The IRAC spectral energy distribution shows a red 8.0–5.8 μm observed color (see Fig. 7), the 8.0 μm observed flux being likely dominated by hot dust heated by the AGN component. Photometric and spectroscopic redshift estimates are in agreement, the former having been obtained with a type-1 AGN template (Polletta et al., in prep.).

It is worth noting that a similar IR SED can be observed also in the case of starburst galaxies at redshift $z = 0.3$–0.5. Actually, in this case a 4.5 μm peak can be produced by the strong 3.3 μm Polycyclic Aromatic Hydrocarbon (PAH) feature lying in IRAC channel-2, while the 8.0 μm flux density is enhanced by mid-IR PAH dust features (6.2, 7.7 μm) at low redshift ($z \leq 0.5$). A good example is given by source EN1_202683 (see Fig. 8), a starburst galaxy at $z = 0.497$. An advantage in breaking this kind of aliasing would be provided by J, H, K band data. In fact the observed $(J - 3.6)_{AB}$ color of a typical starburst (e.g. M 82) is $\sim$0.3 at $z = 0.4$, while it increases to values $>$1.5 at $z \geq 1.4$. Similarly, the $(K_{\rm s} - 3.6)_{AB}$ values are $\sim$−0.4 and $\sim$0.6 at the same two redshifts (see Fig. 9). At $z = 0.4$, the 1.6 μm peak lies in the $K_{\rm s}$ band and the $K_{\rm s}$ flux is brighter than in the IRAC bands. The $K_{\rm s}$ band is gradually shifted blueward of the peak, at increasing redshift, and the $(K_{\rm s} - 3.6)_{AB}$ color changes sign at $z \simeq 0.6$.

Such low-z 4.5 μm-peak-like sources are not reported in Tables 3 and 4, since they do not conform to the IR-peak selection (because their peak is not due to the 1.6 μm feature) and they are easily spectroscopically identified by using bright optical lines.

On the other hand, another source (EN2_275226) shows a clean 4.5 μm-peak, with $S(8.0) < S(4.5)$ and no rise in IRAC channel 4, but the observed UV (restframe) spectrum shows that it hosts a type-1 AGN as well. This object lies at $z = 1.710$, in perfect accordance with the 4.5 μm-peak selection and the photometric redshift estimate. It is likely that the AGN component dominates the UV restframe spectrum, while the near-IR SED is powered mainly by star light.

Finally, source LH_572243 lies at $z = 1.820$, having narrow lines detected in its spectrum. A bright, narrow C IV ($\lambda = 1549$ Å) emission line, without any P-Cyg profile, is detected, testifying to the presence of a type-2 AGN nucleus (e.g. Farrah et al. 2005), which is also confirmed by X-ray data.

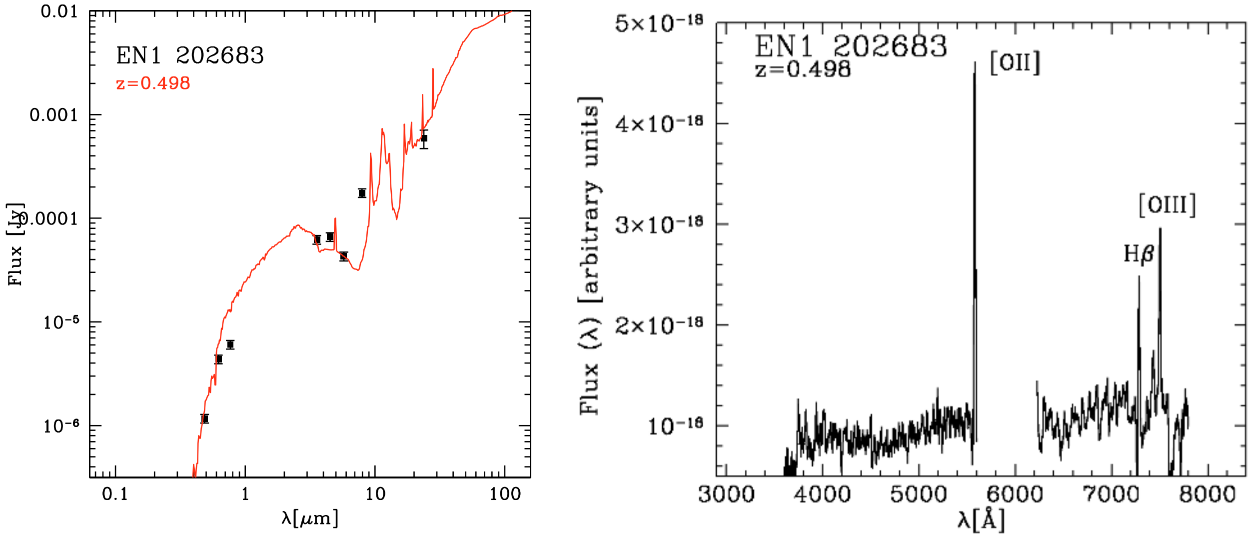

Fig. 8. Example of low-redshift starburst galaxy displaying an IRAC SED which resembles a 4.5 μm peaker. Note that the 8.0 μm flux density is higher than the 5.8 μm, but note also that source EN1_202260 (Fig. 7) has the same property but lies at z = 1.545. The photometric data are compared to the prototypical M 82 starburst template, normalized to the 5.8 μm band.

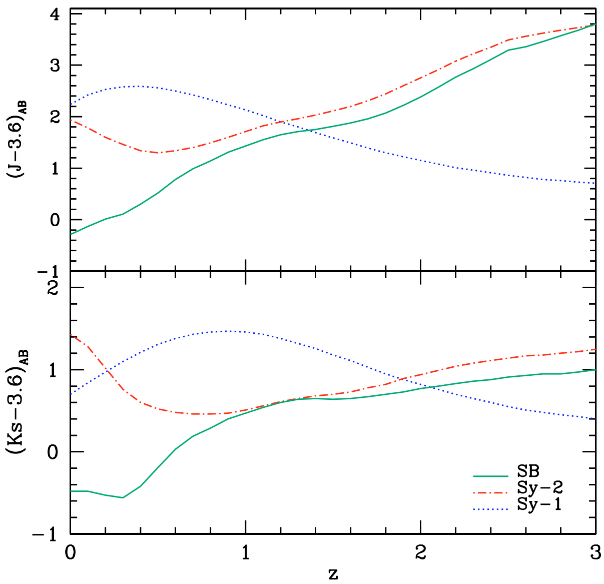

Fig. 9. Trend of JK-IRAC colors, as a function of redshift, as computed for starburst (M 82, Silva et al. 1998), seyfert-2 (IRAS 19254-7245, Berta et al. 2003) and seyfert-1 (Mrk 231, Fritz et al. 2006) templates.

The remaining 4.5 μm-peak targets (LH_245782 and LH_576281) don't have any spectroscopic redshift confirmation, although their continuum emission is detected by LRIS.

As a whole, 6 out of the 8 4.5 μm-peakers have a robust spectroscopic redshift, as derived from emission lines. Considering that LH_245782 was included in one of the two masks observed at high airmass, this translates into a 87.5% successful detection for 4.5 μm peakers. Besides the presence of AGN components, our photometric estimates of redshift were consistent with the actual spectroscopic evidence in 80% of the cases, while for the remaining poor photometry is the main cause of discrepancy.

5.2. 5.8 μm-peak sources

Our masks include 27 5.8 μm-peak targets, of which only 10 have a confirmed spectroscopic redshift. Thirteen out of the 17 without spectral lines detected lie in the Lockman Hole field, whose observing conditions were not optimal for optically-faint objects. The remaining four are all faint targets, having $r' \geq 23.5$.

In the 5.8 μm-peaker sample, we distinguish between sources having a clear stellar 1.6 μm peak detected in IRAC bands (e.g. object EN2_172324, see Fig. 7) and sources with a steep infrared SED (e.g. target EN1_279954, Fig. 7). The latter are likely to be composite sources, whose near-IR emission is not only due to low-mass stars, but also to an AGN component. The 1.6 μm restframe peak is produced by the stellar component, but it is diluted by the AGN emission, which reddens the 5.8–8.0 μm color. These sources are characterized by a very red 5.8–4.5–3.6 μm slope, with flux ratios of $S(5.8)/S(4.5) \simeq 1.4$–1.8 and $S(4.5)/S(3.6) \simeq 1.3$–1.5.

This group consists of targets EN1_205467, EN1_279954 and EN2_165986. For the first one we were not able to derive any spectroscopic redshift, while the other two have very bright, broad ultraviolet emission lines (see Tables 3 and 4), confirming the presence of a type-1 AGN contributing to the optical observed fluxes. The two sources turn out to be at redshifts $z = 2.409$ and $z = 2.163$ respectively, consistent with the 1.6 μm SED feature lying in the 5.8 μm IRAC band. The photometric redshift estimate for this kind of source is carried out by adopting an AGN-like template (Polletta et al., in prep.), which leads to a 50% consistency with the actual spectroscopic measure (see Table 2). This problem can be ascribed mainly to the lack of sharp features in the broad-band SEDs of these sources.

Sources EN1_282078 and EN2_273717 show a bluer slope, with $S(5.8)/S(4.5) \simeq 1.2$ and $S(4.5)/S(3.6) \simeq 1.1$–1.3 and a smooth 5.8 μm peak. These sources turn out to have broad emission lines as well, at lower redshift, namely $z = 1.685$ and $z = 1.800$ respectively. The AGN contribution to the NIR SED of these sources is likely lower than in the previous case, but still non-negligible and clearly visible in the UV-optical domain (restframe). The inconsistency of the spectroscopic redshift value and the 5.8 μm-peak selection – which implies that the restframe 1.6 μm stellar feature is shifted to the IRAC channel 3 at $z > 1.8$ – is discussed below, and interpreted with a non-negligible AGN contribution to IRAC fluxes (Sect. 5.4).

Also in the case of source LH_574364, the IRAC data define a smooth 5.8 μm peak, but the $S(8.0)/S(4.5)$ flux ratio is smaller than unity in this case (while it was larger than 1 in the two classes described above). Narrow MgII and Fe emission lines are detected. The latter suggests the presence of a type-2 AGN. The smoothness of the peak suggests that this galaxy might lie at $z < 1.5$ with the 1.6 μm feature falling shortward of the 5.8 μm band center. In fact the spectroscopic redshift of this galaxy turns out to be $z = 1.474$, consistent with the photometric estimate.

The target EN1_339960 is formally a 5.8 μm-peaker, but its channel 2 and 3 fluxes are comparable, defining a very broad peak in the IRAC SED. The observed spectrum is dominated by a very strong CIV emission with a ~2000 [km s^{-1}] width, at $z = 1.475$, putting it in the AGN-1 spectroscopic class.

Three galaxies have a confirmed redshift between 1.7 and 2.0, narrow Lyα and other emission lines and SED typical of high-redshift starbursts, i.e. EN1_342445, EN2_11091 and EN2_172324. The latter shows a bright CIV narrow line, with no P-Cyg profile, that we interpret as produced by a type-2 AGN. A reddened torus contributes also to the IRAC SED, shifting the peak to the 5.8 μm band (see Sect. 5.4). For the other two sources, not enough spectral features are detected, therefore they are simply classified as "emission line" galaxies.

The highest redshift IR-peaker detected is a a $z = 2.866$ source, EN1_340451, lying at the upper redshift limit of the 5.8 μm-peak selection. This is a very faint optical source, with bright IRAC emission and a weak 24 μm flux. We detect Ly-α, HeII (λ = 1640 Å) and CIII] (λ = 1909 Å) narrow lines. The wavelength coverage of the data has a gap in the range λ = 5500–6150 Å, where CIV (λ = 1549 Å) would fall, but the presence of HeII (with a ionization energy of 54.4 eV, four times that of HI) suggests the presence of a type-2 AGN component.

Finally, it is important to highlight the presence of one outlier: the low redshift interloper LH_572257, at $z = 0.249$. This object is an X-ray source, with soft (0.3–2.5 keV), hard (2.5–8.0 keV) and broad (0.3–8.0 keV) fluxes of 11.01, 26.71 and 35.15×10^{-16} [erg cm^{-2} s^{-1}]. By examining the optical and IRAC postage stamp images in Fig. 10, one can notice that optically the source seems to consist of two different components: a point-like object (likely the X-ray low-z object) and a fuzzy galaxy, ~1.5″ to the north. It is possible that the latter dominates the IRAC SED and effectively is a high-redshift 5.8 μm-peak galaxy lying underneath a low-z source, which instead dominates the optical fluxes. This is confirmed by the Ks band image, where the optically-faint galaxy dominates and the optically-brighter object is significantly fainter. Couples of white squares are over plotted on the z-band and K_s-band images, centered on the two distinct components.

5.3. Sources with no emission line detection

Apart from objects in the Lockman Hole, for which the observing conditions were not optimal (high airmass), there are four IR-peakers with no line detection in the ELAIS fields. In all cases continuum emission is detected; in Tables 3 and 4 we report the wavelength range covered by the detected continuum for each source.

The IR-peakers without line detection lie at the faint end of the r' magnitude distribution of our targets ($r' > 23.5$, see Table 2). Nevertheless, for other comparably faint IR-peak sources a measure of the spectroscopic redshift has been possible. In Fig. 6 (left panel) the r' and 24 μm AB magnitudes of the ELAIS-N1, N2 IR-peakers are compared. The sources without line detection turn out to be those with brighter 24 μm fluxes, of the order of 0.5–1.0 mJy.

The plot on the right shows that these galaxies are also those with the brighter mid-IR excess, i.e. the reddest (3.6–24) μm color. The two reddest ones lie close to a broad-line IR-peaker. One (EN1_205467) of the two shows a power-law IRAC SED (plus 5.8 μm-peak) and is a point-like object on optical images; its photometric redshift is $z = 0.320$, but it is not reliable because of the almost featureless broad-band SED.

The second one (EN2_269695) is a fuzzy galaxy on optical images and shows a sharp 5.8 μm peak. The photometric redshift is $z = 1.800$, which would allow UV emission lines (Lyα, MgII) to be detected in the covered spectral range (see Table 3). The huge mid-IR luminosity suggests that this is a powerful starburst, heavily extinguished by dust, which would also explain the lack of detected emission lines.

The remaining two objects (EN1_341469 and EN2_10334) are the two optically-reddest in the IR-peaker category, with (r' – 3.6 μm) > 4.9 (in AB units, see Fig. 6). These two sources are also the two brightest 24 μm emitters, with $S(24) > 1.0$ mJy.

The photometric redshifts are $z = 1.54$ and 2.01 respectively; by adopting a typical starburst template (e.g. M 82), we derive bolometric infrared (8–1000 μm) luminosities of 5×10^{12} $L_\odot$ for both sources, which would imply an SFR in excess of 800 $M_\odot$/yr (Kennicutt 1998), if powered only by star formation. Such level of activity would produce a Lyα emission of 2.5×10^{11} $L_\odot$.

Unfortunately, for EN1_341469 no blue-arm spectrum is available and we cannot test a possible detection of Lyα. As far as EN2_10334 is concerned, at a redshift $z = 2.01$, that Lyα luminosity corresponds to a flux of $S(\mathrm{Ly}\alpha) = 3.1 \times 10^{-14}$ [erg cm^{-2} s^{-1}] and the line would fall at λ = 3660 Å. The continuum of source EN2_10334 is detected at a 2σ level with a flux of 2.0×10^{-18} [erg cm^{-2} s^{-1} Å^{-1}]. Adopting an intrinsic *FWHM* of 10 Å, in order not to detect the line at a 5σ level, the source must be extinguished by A(Lyα) = 5.75 magnitudes, corresponding to $A_V \simeq 2$ (using the Calzetti et al. 1994 extinction law).

In the case that a type-2 AGN plays a non negligible role in the emission mechanism, then these numbers would significantly change.

5.4. Modeling of observed SEDs

The spectral energy distributions (SEDs) of the IR-peak galaxies with spectroscopic redshifts are analysed here, by means of multi-component fitting.

For sources that do not show any AGN signature in their spectra or broad-band SEDs, we adopt the technique described in Berta et al. (2004) of mixed stellar population synthesis. The observed SEDs are reproduced by combining simple stellar populations (SSPs) of solar metallicity, built on the basis of the Padova 1994 isochrones (for more details on the SSP library see Berta et al. 2004). Each phase in the SSP history is extinguished by a different amount of dust, according to age-selective extinction (Poggianti et al. 2001). Since disc populations are on average affected by a moderate A_V (< 1 mag, e.g. Kennicutt 1992), the maximum allowed absorption for stars older than 1 Gyr is A_V = 0.3–1.0 magnitudes. For younger populations the color excess gradually increases, but is limited to $A_V \leq 5$.

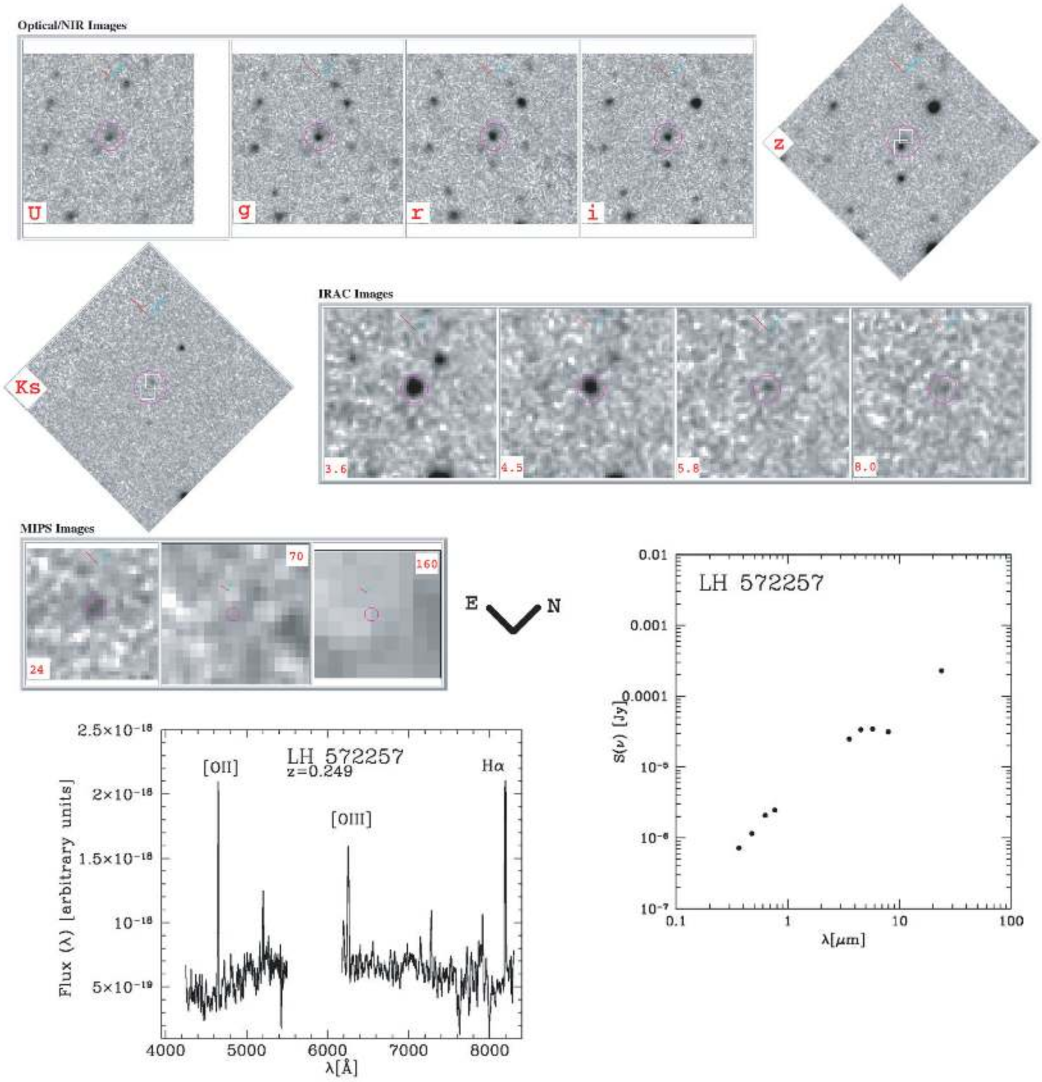

Fig. 10. The 5.8 μm-peak target LH_572257 at $z = 0.249$. White squares are drawn on the z and K_s band stamps, in order to guide the reader in finding the two physical components that contribute to the observed SED (see text for more details). Stamp size is 0.01 deg.

The 24 μm flux is included in the fit and it is used for constraining the amount of dust extinguishing young stars in the ongoing starburst. The energy absorbed by dust at UV-optical wavelengths is reprocessed to the mid- and far-IR domain, by means of a prototypical starburst template.

An M 82 template was adopted, built combining the Silva et al. (1998) model and the Förster Schreiber et al. (2001) observed mid-IR spectrum. Local ultra-luminous sources ($L_{\rm IR} > 10^{12}\ L_\odot$) can be characterized by deep silicate 10 μm self-absorption and "cold" SEDs (e.g. Arp220). Similar templates equally show the usual stellar 1.6 μm peak.

Nevertheless, increasing observational evidence exists that high-z IR-peakers detected in the mid-IR resemble the M 82 prototype. Spitzer mid-IR IRS spectra of $z \simeq 1.9$ IR-peak galaxies (Weedman et al. 2006) are dominated by bright PAH features and lack silicate 10 μm self-absorption. Rowan-Robinson et al. (2005) studied and classified the SEDs of SWIRE sources over 6.5 deg^2 in the ELAIS-N1 field. These authors find that M 82-like starbursts are 3 times more numerous than colder Arp220-like objects. Based on the observed redshift distribution and on number counts modeling, they also infer that this ratio is even higher at $z \sim 1.5$–2.0. Lonsdale et al. (in press) performed 1.2 mm (250 GHz) observations of SWIRE 24 μm-selected (H)ULIRGs with the Max Plank Millimeter Bolometer (MAMBO, Kreysa et al. 1998) on the IRAM/30 m telescope. As a result, they find that the 1.2 mm/24 μm flux ratio of these sources resembles that of M 82, lower than for an Arp220-like population, and lower than what found for sub-mm selected galaxies (SMGs). It is worth noting, in fact, that their selection (similar to ours) favors 24 μm-bright systems, instead of mm-bright objects. All of these recent findings drove the choice of the M 82 template, as stated above.

As a further check, we have attempted stacking of far-IR (70 and 160 μm) SWIRE images at the position of the observed IR-peakers, but unfortunately no signal was detected on the stacked frames.

Also the detected spectroscopic features have been included in the fitting procedure, in order to provide additional constraints on the star formation history of these sources.

Table 7 reports the results of this analysis: for each source, the best fit stellar mass and ongoing star formation rate (SFR) are listed. The SFR is computed as an average on the last 10^8 yr in the life of the galaxy, in order to be comparable to the Kennicutt (1998) calibrations. We also report the derived extinction, as

Table 7. Results of spectro-photometric fitting for sources with no AGN component. The five columns on the right contain the stellar masses of galaxies, their ongoing (within the last 10^8 yr) star formation rate, two values of the intrinsic extinction, and the IR (8–1000 μm restframe) luminosity produced by the ongoing starburst, estimated assuming an M 82-like template. The two A_V values are computed by averaging over the whole galaxy life and over the last 10^8 yr (representing the amount of dust affecting the ongoing burst). In parenthesis the 3σ ranges derived from the exploration of the parameter space are reported.

ID SWIRE	Type phot.	Class spec.	z spec.	Mass($\star$) [10^{11} $M_\odot$]	SFR(10^8 yr) [$M_\odot$/yr]	A_V(mean) [mag]	A_V(10^8 yr) [mag]	L_{IR} [10^{11} $L_\odot$]
EN1_202261	P2	ELG	1.339	1.44 (1.41–2.36)	489 (171–741)	1.68 (1.29–1.73)	1.82 (1.71–1.88)	10.81 (8.48–12.84)
EN1_342445	P3L	ELG	1.917	1.04 (0.91–1.84)	426 (268–480)	1.10 (0.57–1.17)	1.40 (0.96–1.49)	9.37 (6.89–12.81)
EN1_340451	P3	NLAGN	2.866	6.69 (6.12–7.29)	56.1 (29.6–106)	0.63 (0.41–0.76)	2.18 (1.43–2.32)	36.79 (25.45–50.58)
EN2_11091	P3L	ELG	1.946	3.94 (2.37–4.20)	208 (197–575)	0.61 (0.29–0.89)	0.80 (0.71–1.82)	16.13 (10.58–20.94)
EN2_167372	P2L	ELG	1.445	2.62 (2.08–2.77)	86.9 (25.4–192)	0.59 (0.07–0.93)	1.34 (0.35–1.80)	4.98 (0.96–12.77)
EN2_166134	P2	ELG	1.337	3.40 (3.05–3.86)	17.9 (9.90–200)	0.79 (0.50–0.89)	1.65 (1.20–2.02)	9.06 (5.82–12.41)
LH_572243	P2,X	NLAGN	1.820	0.91 (0.85–0.92)	34.3 (27.7–91)	0.82 (0.79–0.90)	2.09 (1.99–2.28)	9.27 (9.04–10.51)

Table 8. Results of SED fitting for IR-peakers requiring an AGN component. The fit consists in the combination of a simple stellar population and a torus model (Fritz et al. 2006). The 3σ ranges for the main geometrical and dust properties of the torus are reported, as well as stellar population ages, extinctions and masses.

ID	Type	Class	z	Torus						Stellar population			Total	% AGN	
SWIRE	phot.	spec.	spec.	$\frac{R_{out}}{R_{in}}$	$\Theta^\dagger$	$\tau_{9.7}$	$\Psi^\ddagger$	L_{BH}	α	age	$E(B-V)$	Mass	L_{IR}	8.0 μm	IR
					[deg]		[deg]	[10^{45} $L_\odot$]	index*	[10^6 yr]	[mag]	[10^{10} $M_\odot$]	[10^{11} $L_\odot$]		
EN1_202260	P2,X	BLAGN	1.545	100–300	100–140	0.6–2.0	0–30	0.79–1.58	–1.0	50–300	0.2–0.4	3.98–10.0	4.23–7.05	53–71%	10–62%
EN1_282078	P3	BLAGN	1.685	20–100	60–100	6.0–10.0	0–60	1.58–3.16	–1.0	50–100	0.6–0.8	3.98–6.31	10.4–23.7	53–65%	2–40%
EN1_279954	P3,pow	BLAGN	2.409	30–100	60–140	0.6–3.0	0–50	1.58–3.16	–0.5	10–100	0.6–1.0	2.51–15.8	15.4–27.1	49–63%	5–31%
EN1_339960	P3	BLAGN	1.475	30–100	60–140	0.6–1.0	0–50	0.20–0.32	–1.0	50–500	0.2–0.6	3.98–25.1	3.83–5.50	39–49%	10–48%
EN2_275226	P2	BLAGN	1.710	30–100	100–140	1.0–6.0	0–20	0.32–1.58	–0.5	10–50	0.6–0.8	1.58–2.51	15.3–26.1	37–54%	1–20%
EN2_273717	P3	BLAGN	1.800	30–100	100–140	0.3–3.0	0–20	1.00–2.51	–0.5	10–50	0.6–0.8	1.00–2.51	26.4–38.2	48–62%	2–24%
EN2_172324	P3	NLAGN	1.739	30–100	60–140	0.3–2.0	40–90	1.00–3.16	–1.0	50–100	0.4–0.6	15.8–25.1	16.4–23.4	32–45%	3–39%
EN2_165986	P3,pow	BLAGN	2.163	20–100	80–140	3.0–10.0	30–50	3.16–10.0	–1.0	10–100	0.2–0.6	1.00–10.0	11.5–18.6	64–80%	20–53%
LH_574364	P3,R	NLAGN	1.474	100–300	100–140	0.3–3.0	30–70	1.58–1.99	–0.5	50–100	0.4–0.8	2.51–6.31	7.42–9.01	55–63%	30–77%

† The aperture angle Θ is computed starting from the equatorial plane, and it is doubled, accounting for equatorial symmetry.
‡ The viewing angle Ψ is computed starting from the polar axis.
* Source power law slope in UV-optical-IR range ($\lambda L[\lambda] \propto \lambda^\alpha$).

averaged over the whole galaxy life and over the last 10^8 yr, as well as the bolometric IR (8–1000 μm) luminosity, as computed with the adopted template. Finally, 3σ ranges, as computed from the exploration of the parameters space, are listed within parentheses. A detailed description of degeneracies is provided in Berta et al. (2004). The average number of SSPs effectively involved in the fit is 3–4, depending on redshift.

In Fig. 7 we show the fit to the observed SEDs. The blue-dashed and red-dotted lines represent the contributions of young (age $< 10^9$ yr) and old (age $\geq 10^9$ yr) stars to the modeled SEDs. The green solid line is the total emission in the optical, while the long-dashed cyan line longward of 5 μm (restframe) is the M 82 template. The integral of the template between 8 and 1000 μm reproduces the absorbed energy in the UV-optical. On the plots, we report the χ^2 values (not reduced), the stellar mass and the fraction of mass in young/old stars.

The IR-peak sources fitted in this way turn out to be powered by strong starburst activity, with SFRs reaching 400 $M_\odot$/yr and IR luminosities exceeding 10^{12} $L_\odot$ in the most powerful cases. The observed SEDs are overall well reproduced over the whole spectral domain from the U band to 24 μm, with reduced χ^2 between 1 and 2 (see Berta et al. 2004, for a discussion on high χ^2_ν values).

The LRIS spectrum of source LH_572243 shows a weak, but clear, Civ emission, with no P-Cyg profile, which we interpreted as due to AGN activity. The stellar synthesis fit, however, reproduces the observed SED without the need of any type-2 AGN component. Similarly, we classified source EN1_340451 as a type-2 AGN, on the basis of the HeII narrow line detected with Keck, but its broad-band SED is well fitted by a stellar model, with no need for additional components. Thus this source is best fitted by a moderate starburst (SFR = 56.1 $M_\odot$/yr) hosted in an extremely massive galaxy with $M = 6.69 \times 10^{11}$ $M_\odot$.

A detailed analysis of the stellar mass function of IR-peak sources is being carried out for the SWIRE survey, and is deferred to Berta et al. (in prep.), which will take into full account the spectroscopic results presented here.

As far as sources with an AGN spectral classification are concerned, a different fitting procedure was adopted. We reproduced the observed datapoints by means of the combination of a simple stellar population and a torus template (Fritz et al. 2006). The purpose, in this case, is to show how the detected IR-peak can be reproduced with multiple components, when the spectroscopic redshift is not fully consistent with what was expected for a pure stellar 1.6 μm peak.

We have therefore combined the Fritz et al. (2006) torus library, with the simple stellar population library used before (Poggianti et al. 2001; Berta et al. 2004). The best fit is sought by χ^2 minimization. The stellar component consists of one SSP, extinguished by a varying amount of dust. Again, extinction is also constrained through a far-IR starburst template. In combination to stars, the torus AGN emission is added, in order to fit the observed data.

The torus library by Fritz et al. spans several geometries of the toroidal dust distribution around the central AGN nucleus, varying the ratio between outer and inner radii (R_{out}/R_{in} = 20–300), and the aperture angle of the torus (measured starting from the equatorial plane, Θ = 40°–140°). We limit our analysis to a uniform dust distribution in the torus, because we do not have sufficient data points to constrain the entire library and because our purpose here is to get a general requirement on the level of AGN contribution to the mid-IR SED. The optical depth at the equator covers the range τ = 0.1–10.0 at 9.7 μm. The spectrum emitted by the central engine is modeled with a broken power-law $\lambda L(\lambda) \propto \lambda^{\alpha}$, with indexes α = 1.2, 0, −0.5 in the ranges λ = 0.001–0.03, 0.03–0.125, 0.125–20 μm respectively. Two different sets of models are included, differing for the UV-optical-IR slope of this power law, being $\alpha = -0.5$ or $\alpha = -1$. See Fritz et al. (2006) for more details of this model.

The results of this AGN+stars fit are in Table 8 and plotted in Fig. 7. The green dashed line represents the stellar component (including starburst dust), the blue dotted line is the AGN contribution to the global SED (red solid line).

The details of the best fit models are subject to strong degeneracies and are limited by the use of one single SSP, instead of a sophisticated model like in the starburst case. A unique best fit can not be achieved due to the limited photometry, therefore 3σ ranges for the parameters are reported in Table 8, instead of best fit values. These fits have the illustrative purpose to point out how the shape of the broad band SED of IR-peak galaxies with AGN detection in the UV restframe spectra can be simply explained by two different physical components.

According to the unified scheme for AGN emission (Antonucci & Miller 1985), in the UV type-1 features emerge when the viewing angle does not intercept the dusty torus. At longer wavelengths, stellar and AGN spectral energy distributions are complementary, with the stellar component peaking around 1 μm and dominating the optical spectrum, while the torus warm dust emission increases longward and dominates the 3–10 μm range (see, for example, source EN1_202260). The warm component of the torus, coming from the inner regions closer to the central engine, can significantly contribute to the IR-peak itself, modifying its shape and apparently shifting it to a wavelength longer than 1.6 μm (restframe). A good example of this effect is source EN1_282078, for which the IR-peak is detected in the restframe K band.

When a type-2 AGN is present, which in fact happens only in three of our sources, the UV-optical SED can be easily fitted by stars alone. In two cases (EN1_340451 and LH_572243) the whole SED, up to the mid-IR is reproduced with a simple starburst model (see above). Only in one case (EN2_172324) is a warm dust component needed in order to explain the near-IR fluxes. Nevertheless, in this latter case, our code cannot fully reproduce the observed shape of the IR-peak, even including the type-2 AGN.

Other effects might explain the observed SED of EN2_172324. Dust in AGB stars can significantly modify the shape of the IR-peak, changing its colors. The feature flattens, becoming bluer on the blue side and redder on the red side (see Piovan et al. 2003), and the H^- feature is smoothed. Nevertheless these effects cannot explain a shift in the redshift of the peak of Δz = 0.4, as apparently observed in source EN2_172324.

At the observed redshift (z = 1.739), both Brγ and Paα fall in the 5.8 μm IRAC channel and could give a significant contribution to the observed flux, if very strong. Obviously, as a final source of uncertainty, photometry plays an important role.

Finally, blind tests on the sources listed in Table 7 (i.e. with no evidence for an AGN in their spectra) were carried out, using the multi-component approach. The fit confirm that a possible AGN would contribute less than 2% to the IRAC fluxes of these objects.

6. Other interesting sources

The multi-object mask geometry, and the low density of IR-peakers on the sky, allowed us to target several SWIRE/Spitzer sources having peculiar properties or multiwavelength counterparts over a wide fraction of the electromagnetic spectrum.

The properties of some of these interesting sources are briefly described here, while a detailed analysis is deferred to subsequent papers.

6.1. High-redshift AGNs

The observed masks include three type-1 AGNs at redshift $z > 2.5$. Two of these AGNs (EN1_282051 and EN2_274735) were selected as $z \sim 3$ QSO candidates by their flux decrement in the U-band. We further required a red IRAC color ($m[3.6] - m[4.5] > -0.15$) which eliminates contamination from main sequence stars (Siana et al. 2007, in prep.).

The third object (EN1_202756) did not have any particular priority; it would have been selected as a $z \sim 3$ QSO but since it is fainter ($g' > 23.42$, Vega), the U band depth was insufficient to provide a red enough $U - g'$ limit for selection. This AGN is not detected at 24 μm, nor in IRAC channels 3 and 4, in the SWIRE survey.

EN1_282051 is a bright quasar, with a 24 μm flux of 740 μJy, lying at redshift z = 3.1. Four broad emission lines were detected: Lyβ, Lyα, CIV (λ = 1549 Å) and CIII] (λ = 1909 Å). Figure 11 shows the observed spectrum and the SED of this target. The latter has been superimposed with two different QSO templates differing in the FIR/optical luminosity ratio. The optical part of the templates belongs to the composite quasar spectrum from the Large Bright Quasar Survey (Brotherton et al. 2001) while the infrared section was obtained as the average SED of SWIRE quasars (Polletta et al. 2006; Hatziminaoglou et al. 2005). A detailed analysis of this object is being carried out by Siana et al. (in prep.).

Five broad emission lines were detected for target EN2_274735, Lyα, SiIV,OIV] (λ = 1400 Å), CIV (λ = 1549 Å) and CIII] (λ = 1909 Å), at redshift z = 2.605, with several intervening systems producing absorption lines. This object is a optically-bright quasar that is not detected in the SWIRE 24 μm survey (at the 200 μJy limit) and has a FIR/optical color redder than in the previous case (see Fig. 11). Further analysis is deferred to Siana et al. (in prep.).

Finally, EN1_202756 is a faint quasi stellar object, with a r' magnitude of 22.95 (AB), detected only in the 3.6 and 4.5 μm channels, with a 16.65 and 17.12 μJy flux respectively. Six emission lines are detected at z = 3.005: Lyβ, Lyα, CIV, HeII (λ = 1640 Å), NIII] (λ = 1750 Å) and CIII]. The observed colors are redder than the QSO templates adopted (see Fig. 11).

6.2. X-ray sources

Two masks were centered on the Lockman Hole and ELAIS-N1 regions which had been observed in the X-rays by Chandra (Polletta et al. 2006; Manners et al. 2003, 2004; Franceschini et al. 2005).

In the Lockman Hole, three X-ray sources were put on a slit, a 4.5 μm-peaker (already discussed in Sect. 5.1), the troublesome 5.8 μm-peak object LH_572257, which turned out to be a low-redshift confused interloper (see Sect. 5.2), and finally the low-redshift (z = 0.355) type-1 AGN LH_575325, discussed in Wilkes et al. (in prep.).

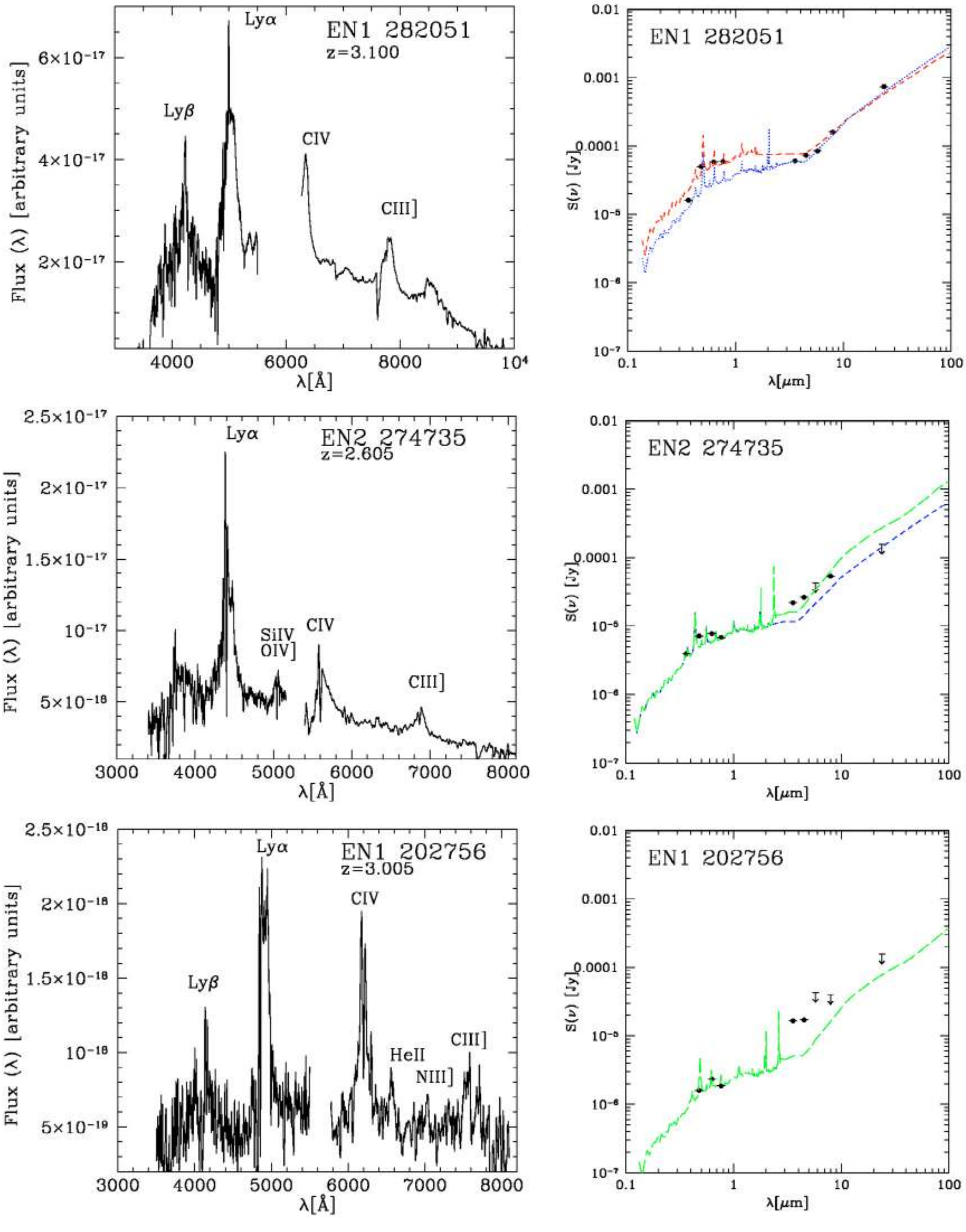

Fig. 11. Spectra and SEDs of high-redshift QSOs. The observed photometry is compared to three different templates. The standard template (dotted lines) is built with the optical composite quasar spectrum from the Large Bright Quasar Survey (Brotherton et al. 2001) and the average SED of SWIRE quasars (Hatziminaoglou et al. 2005). The reddest (long-dashed lines) and bluest (short-dashed) differ from it only in in their IR/optical luminosity ratio (Polletta et al. 2006).

As far as ELAIS-N1 is concerned, four X-ray sources have a confirmed spectroscopic redshift. Two sources have typical type-1 AGN spectra (EN1_204120 and EN1_202260, z = 1.475, 1.545), consistent with the classification by Franceschini et al. (2005); EN1_203962 is a type-2 AGN at $z = 0.874$, while finally EN1_201165 has a starburst spectrum with [OII] and CaII-HK detected at $z = 0.762$. Franceschini et al. (2005) classify both targets as Seyfert-2 galaxies, although the latter (target 92 in their work) shows a lack of X-ray photons with respect to the AGN prediction.

7. Discussion

When neither broad lines, nor type-2 lines are present in the spectra of the observed IR-peakers, a pure stellar spectrophotometric synthesis was performed (Berta et al. 2004). Seven sources satisfy these requirements; their luminosities are in (or close to) the ULIRG regime ($L_{IR} \geq 10^{12}$ $L_{\odot}$), and their bright IR fluxes turn out to be powered by strong obscured starburst activity. The median rate of star formation is ~90 [$M_{\odot}$/yr]; the median extinction of the stars in the starburst (age $\leq$ 10^8) is $A_V = 1.65$ mag (see Table 7).

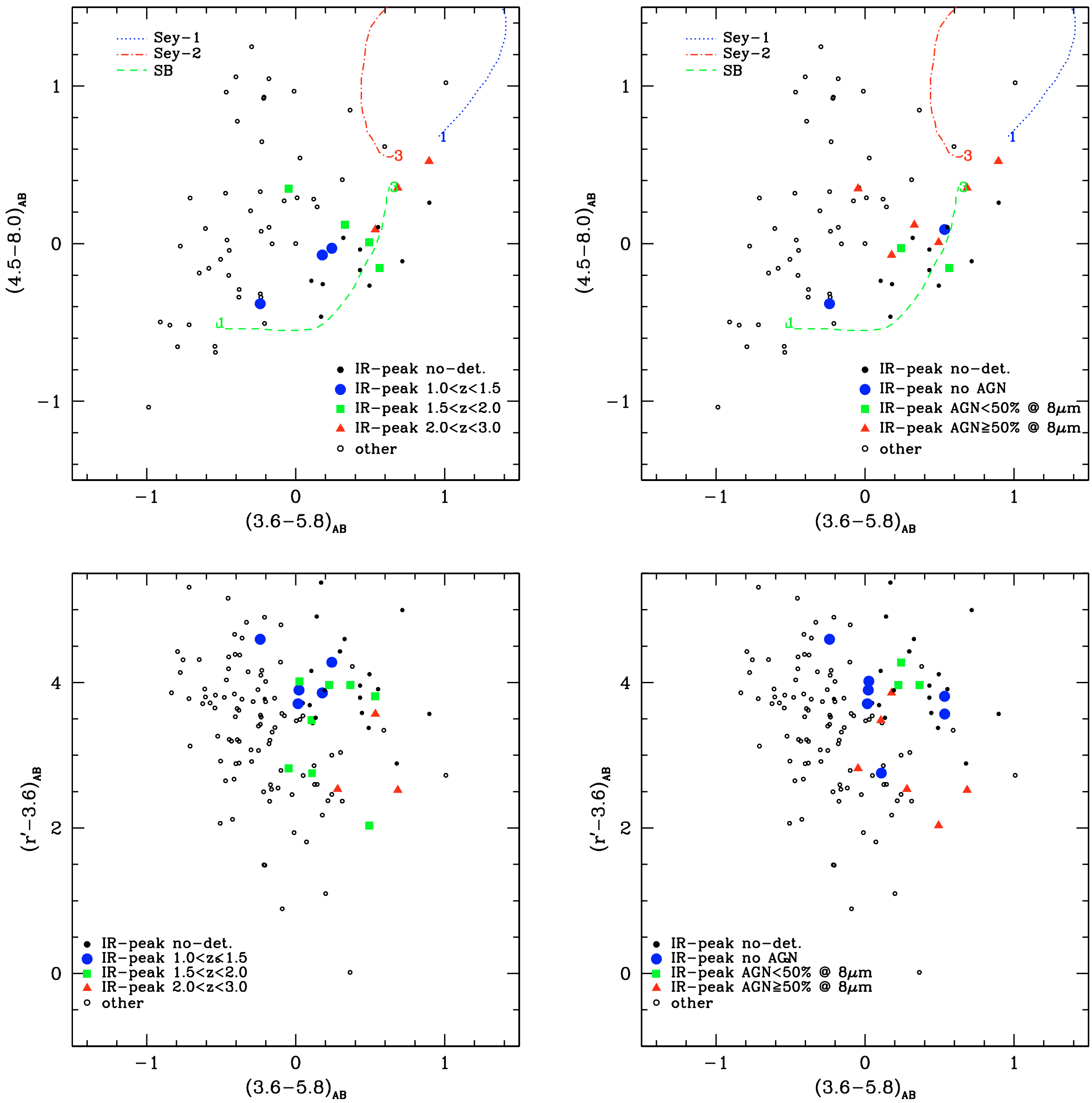

Fig. 12. Color–color plots of the targets with spectroscopic redshifts. The datapoints for IR-peak galaxies (detected in the required bands) are color-coded by redshift (*left*) and AGN torus contribution at 8.0 μm (*right*). Three template tracks from $z = 1$ to $z = 3$ are shown: a starburst (dashed lines, M 82, Silva et al. 1998), a seyfert-2 (dot-dash, IRAS 19254-7245, Berta et al. 2003) and a type-1 AGN (dotted, Mrk 231, Fritz et al. 2006).

The host galaxies of these starbursts are extremely massive, $M(\star) = 1$–6×10^{11} $M_{\odot}$, at redshifts $z = 1.3$–2.8. Consequently, the median derived timescale for star formation $t_{SF} = M(\star)/SFR$ turn out to be 2.6×10^9 years, requiring many such episodes of star formation in order to form the whole assembled mass (provided that the typical duration of a starburst episode is $\sim 10^8$ yr). The two most active objects, with *SFR* of the order of 500 $M_{\odot}$/yr, have $t_{SF} \sim 2$–3×10^8 yr, fast enough to form the bulk of the total stellar mass in one single extreme burst of star formation.

A different approach to SED fitting is followed, when dealing with sources that show AGN signatures in their spectra or SEDs (seven out of 16 targets). In this case, we combine a single SSP and a torus model (Fritz et al. 2006).

The results show how warm dust from an AGN torus can be a significant contributor to IRAC fluxes, especially to channels 3 and 4, for example providing a fraction >50% of the total emission at 8.0 μm. It is very interesting to point out that in these cases the AGN component not only dilutes the infrared stellar peak, but also produces an apparent shift of the peak to longer wavelengths. This effect is basically due to the shape of the Planck emission of warm dust at temperatures of few to several hundreds Kelvin. The presence of an AGN is sufficient to explain the inconsistency between spectroscopic and photometric redshifts of IR-peakers.

In type-1 objects, the AGN component dominates the UV restframe emission, producing bright broad lines in the observed spectra; in the optical-near-IR domain stars and torus

SED are complementary, and stars provide the bulk of the observed fluxes. The torus component again emerges at longer wavelengths, in the near-mid infrared, with warm dust from the inner regions dominating between 3–10 μm restframe.

The best fit solutions preferentially require a small torus distribution of dust around the central AGN, with $R_{\rm out}/R_{\rm in} = 30$–100. The AGN component dominates in the IRAC observed frame, but the fraction of flux due to the AGN decreases at longer wavelengths. In more than 50% of cases, the torus usually does not significantly contribute to MIPS fluxes (e.g. at 24 μm) and the contribution to the total IR (8–1000 μm) luminosity is ~15% for the majority of sources (see Table 8). Therefore the mid-IR spectrum of IR-peak galaxies is expected to be characterized by bright PAH features. Weedman et al. (2006) confirm the presence of bright 7–13 μm PAHs in the IRS spectra of optically-faint 5.8 μm-peak galaxies, with no evidence of dilution by AGN torus dust in 90% of the examined cases. This suggests that the mid-IR emission of Weedman's galaxies is dominated by starburst activity. Nevertheless, their sources lie at $z \simeq 1.9$, on the lower bound of the 5.8 μm selection; even in the case of these optically-faint sources, it is possible that an AGN (torus) component provides a non negligible contribution to IRAC fluxes, without being identified in the mid-IR.

All the sources with type-1 AGN broad lines detected in the Keck spectra require a non negligible contribution of torus warm dust to their IRAC SEDs (see Table 8), while two objects with type-2 AGN classification can be fitted with a stellar component only, with no needs of any torus to reproduce the observed IRAC fluxes. Conversely, all sources showing a significant excess in the IRAC domain, with respect to pure stellar emission, show AGN signatures in their UV-optical restframe spectra (either type-1 or 2).

Figure 12 shows the distribution of the IR-peak galaxies with a confirmed spectroscopic redshift, in optical-IRAC color space. The points belonging to IR-peakers are color coded by redshift (left panels) and by torus contribution at 8.0 μm (right panels). Redshift tracks for a Seyfert-1 (Mrk231, Fritz et al. 2006), a Seyfert-2 (IRAS 19254-7245, Berta et al. 2003) and a starburst (M 82, Silva et al. 1998) template are shown.

At comparable IRAC fluxes, the observed sources need to be increasingly optically blue with redshift (bottom left panel), in order to be detected by Keck/LRIS, with reasonable exposure times. IRAC colors (top left) change in the same direction as the starburst track (which is dominated by stars in the near-IR), but show a significant scatter, due to the torus contribution to the SEDs. At the highest redshift end ($z \geq 2.4$), the IRAC SED becomes flatter and resembles a power-law with a very diluted 1.6 μm peak. The $S(8.0)/S(4.5)$ flux ratio exceeds unity and sources transit to the AGN locus in the IRAC color space (triangles in the top left plot of Fig. 12).

As far as the torus contribution to the 8.0 μm observed flux is concerned (right panels), the properties of the observed sources are not easily identified with the use of broad band colors only. No clear trend of the AGN fraction is seen in the IRAC color plot (top right, Lacy et al. 2004), for IR-peak galaxies, nor is segregation of different type of sources seen. Apart from a couple of sources with power-law like SEDs (compare to. Fig. 2), the IR-peak galaxies hosting an AGN tend to lie in the same locus of starburst galaxies in the IRAC color space. The AGN contribution to IRAC SEDs has been identified:

1. through the presence of broad emission lines in their UV-optical spectra;
2. thanks to spectroscopic redshifts lower than expected, requiring a non negligible torus component taking part in the near-IR emission of IR-peakers.

In the optical, sources with 8.0 μm torus fraction larger than 50% seem to be preferentially bluer than the others, as expected when the type-1 AGN component increasingly emerges at UV wavelengths (restframe). Type-2 AGNs show optical-IR colors similar to starbursts, as their SEDs can even be fitted by stars alone.

The "AGN IR-peak population" contaminates the overall sample and is difficult to identify on the basis of broad band photometry alone. Extreme care should be taken in the analysis of sources in the fourth quadrant of the IRAC color plot, the best way to break degeneracies and aliases being – of course – spectroscopic confirmation of their physical properties.

8. Conclusions

High redshift galaxies can be identified on the basis of of their restframe near-IR spectral energy distribution. In this spectral domain, low-mass stars dominate galaxy emission, and produce a peak at 1.6 μm (restframe), which is further enhanced by a minimum in the H^- opacity in stellar atmospheres. The stellar peak is detected in the IRAC channels 2 and 3 at redshifts between 1.5 and 3.0.

We have performed Keck/LRIS optical spectroscopy of high-z "IR-peak" galaxies, selected in SWIRE northern fields. In order to be observable with Keck/LRIS, the sample was restricted to the optically brightest sources among the IR-peaker population. A total of 35 such object were targeted, and 16 have a spectroscopic confirmation, in the $z = 1.3$–2.8 range. Among these, six are 4.5 μm-peakers, and the remaining 10 peak at 5.8 μm.

By combining the spectroscopic analysis and broad band SED fitting, we have extended our knowledge in the emission properties of IR-peak objects. The main results that have been described throughout this paper are summarized below and in Table 9.

- The IRAC IR-peak galaxies turn out to lie in the redshift range $z = 1.3$–2.8, broadly confirming expectations. Photometric and spectroscopic redshift are in better accordance for 4.5 μm-peak objects than for 5.8 μm peakers, which turn out to be at slightly lower redshift than expected.
- Low-redshift starburst interlopers represent a significant source of contamination of the 4.5 μm-peak sample. A bright 3.3 μm PAH feature can significantly contribute to the IRAC channel 2 flux, for $z \sim 0.4$. Nevertheless, JHK data can break this aliasing, sources with $(K_{\rm s} - 3.6)_{AB} \leq 0$ being at $z \leq 0.6$.
- The optically-faintest IR-peakers that have very bright 24 μm fluxes turn out to be heavily extinguished starbursts, with $SFR > 500\ M_\odot$/yr and $A_{\rm V} \geq 2$ mag. No emission line are detected in these cases.
- 69% (11/16) of the IR-peakers with spectroscopic confirmation show AGN signatures in their spectra; 64% (7/11) of these are broad-line type-1 objects, the remaining are type-2's. The observed sample biased to the optically-brightest IR-peakers in the sky, likely favoring those which host optically-bright AGN.
- On the basis of SED synthesis and spectral analysis, the 32% (5/16) non-AGN sources are powerful starbursts with SFR as high as ~500 $M_\odot$/yr, stellar masses $M = 1$–$6 \times 10^{11}\ M_\odot$, and extinctions $A_{\rm V} = 1$–2 mag. The most active galaxies have specific SFRs fast enough to produce the bulk of the assembled stellar mass (~$10^{11}\ M_\odot$) in one single burst of star formation.

Table 9. Summary of results.

	No.	%
Observed slits	235	–
Original targets	233	–
Serendip. targets	68	–
Total targets	301	–
Tot. measured redshifts	174/301	58%
Serendip. redshifts	35/68	52%
SWIRE redshifts	150	–
Absorption line glxs	7/150	5%
Emission line glxs	122/150	81%
Starbursts	39/150	26%
Type-2 AGNs	5/150	3%
Type-1 AGNs	17/150	11%
$z > 2.5$ QSOs	3/150	2%
Obs. IR-peakers	35	–
Obs. 4.5 μm-peakers	8/35	23%
Obs. 5.8 μm-peakers	27/35	77%
IR-p. with redshift	16/35	46%
4.5 μm-p. with redshift	6/8	75%
5.8 μm-p. with redshift	10/27	37%
AGN IR-peakers	11/16	69%
Type-1 AGN IR-peakers	7/11	64%
Type-2 AGN IR-peakers	4/11	36%
Type-1 AGN 4.5 μm-peakers	2/7	29%
Type-1 AGN 5.8 μm-peakers	5/7	71%
Type-2 AGN 4.5 μm-peakers	1/4	25%
Type-2 AGN 5.8 μm-peakers	3/4	75%

– All IR-peak broad-line AGN require a non-negligible contribution of torus warm dust to their IRAC SEDs; moreover, all sources that need a torus contribution to their mid-IR SED show AGN signatures in their UV-optical restframe spectra.
– The AGN warm dust contribution to IRAC SEDs produces the apparent shift of the infrared peak longward of 1.6 μm (restframe), highlighted by the non perfect agreement between photometric and spectroscopic redshifts. In fact, the photometric estimate of redshift, based on stellar models, turned out to be frequently overestimated.
– While IR-peakers follow a defined redshift track in the IRAC and optical-IR color space (although with large scatter), the AGN contamination of the sample can not be recognized on the basis of broad band colors only.
– The AGN torus component is important in the IRAC domain, but it usually does not contribute significantly to longer wavelength mid-IR fluxes; hence the mid-IR spectrum of these sources is dominated by PAH features, as confirmed by Weedman et al. (2006) IRS spectroscopy.

Finally, multi-object spectroscopy allowed us to include many other SWIRE sources on slits, for a total of 301 objects. Among these, 174 objects have a spectroscopic redshift; 150 targets with redshift have a SWIRE counterpart. Our slits include 7 X-ray sources, 12 radio sources and 19 IRAC power-law galaxies. On the basis of spectral properties, we have identified 122 narrow-line emission galaxies, 39 turn out to be starbursts and 5 are type-2 AGNs. Seven targets have absorption lines only, 17 are broad-line type-1 AGNs and four are stars. Three high-redshift ($z \geq 2.5$) QSOs complete the view of the targeted zoo.

Acknowledgements. We wish to thank the Keck night staff for their availability in producing calibration frames at the science targets ALT,AZ positions. We are grateful to M. Meneghetti for tests on a supposed gravitational lens (which turned out not to be). We thank A. Bressan and C. Chiosi for useful discussions on UV and near-IR spectral features, S. Ciroi for suggestions on optical spectral classification, F. Di Mille and S. Siviero for elucidation on spectrographs and optical paths.
The Spitzer Space Telescope is operated by the Jet Propulsion Laboratory, California Institute of Technology, under contract with NASA. SWIRE was supported by NASA through the SIRTF Legacy Program under contract 1407 with the Jet Propulsion Laboratory.

References

Allen, M. G., Dopita, M. A., & Tsvetanov, Z. I. 1998, ApJ, 493, 571
Antonucci, R. R. J. & Miller, J. S. 1985, ApJ, 297, 621
Babbedge, T. 2004, Ph.D. Thesis
Baldwin, J. A., Phillips, M. M., & Terlevich, R. 1981, PASP, 93, 5
Berta, S., Fritz, J., Franceschini, A., Bressan, A., & Pernechele, C. 2003, A&A, 403, 119
Berta, S., Fritz, J., Franceschini, A., Bressan, A., & Lonsdale, C. 2004, A&A, 418, 913
Bertin, E. & Arnouts, S. 1996, A&AS, 117, 393
Bolzonella, M., Miralles, J.-M., & Pelló, R. 2000, A&A, 363, 476
Brotherton, M. S., Tran, H. D., Becker, R. H., et al. 2001, ApJ, 546, 775
Calzetti, D., Kinney, A. L., & Storchi-Bergmann, T. 1994, ApJ, 429, 582
Chapman, S. C., Smail, I., Blain, A. W., & Ivison, R. J. 2004, ApJ, 614, 671
Cole, S., Lacey, C. G., Baugh, C. M., & Frenk, C. S. 2000, MNRAS, 319, 168
Cole, S., Percival, W. J., Peacock, J. A., et al. 2005, MNRAS, 362, 505
Dessauges-Zavadsky, M., Pindao, M., Maeder, A., & Kunth, D. 2000, A&A, 355, 89
Dickinson, M., Giavalisco, M., & The Goods Team. 2003, in The Mass of Galaxies at Low and High Redshift, ed. R. Bender & A. Renzini, 324
Dole, H., Lagache, G., Puget, J.-L., et al. 2006, A&A, 451, 417
Egami, E., Dole, H., Huang, J.-S., et al. 2004, ApJS, 154, 130
Eisenhardt, P. R., Stern, D., Brodwin, M., et al. 2004, ApJS, 154, 48
Elbaz, D., Cesarsky, C. J., Chanial, P., et al. 2002, A&A, 384, 848
Ellis, R. S., Smail, I., Dressler, A., et al. 1997, ApJ, 483, 582
Farrah, D., Serjeant, S., Efstathiou, A., Rowan-Robinson, M., & Verma, A. 2002, MNRAS, 335, 1163
Farrah, D., Surace, J. A., Veilleux, S., Sanders, D. B., & Vacca, W. D. 2005, ApJ, 626, 70
Farrah, D., Lonsdale, C. J., Borys, C., et al. 2006, ApJ, 641, L17
Fazio, G. G., Ashby, M. L. N., Barmby, P., et al. 2004a, ApJS, 154, 39
Fazio, G. G., Hora, J. L., Allen, L. E., et al. 2004b, ApJS, 154, 10
Förster Schreiber, N. M., Genzel, R., Lutz, D., Kunze, D., & Sternberg, A. 2001, ApJ, 552, 544
Franceschini, A., Aussel, H., Cesarsky, C. J., Elbaz, D., & Fadda, D. 2001, A&A, 378, 1
Franceschini, A., Berta, S., Rigopoulou, D., et al. 2003, A&A, 403, 501
Franceschini, A., Manners, J., Polletta, M., et al. 2005, AJ, 129, 2074
Fritz, J., Franceschini, A., & Hatziminaoglou, E. 2006, MNRAS, 366, 767
Genzel, R. & Cesarsky, C. J. 2000, ARA&A, 38, 761
Granato, G. L., De Zotti, G., Silva, L., Bressan, A., & Danese, L. 2004, ApJ, 600, 580
Hatton, S., Devriendt, J. E. G., Ninin, S., et al. 2003, MNRAS, 343, 75
Hatziminaoglou, E., Pérez-Fournon, I., Polletta, M., et al. 2005, AJ, 129, 1198
Hauser, M. G., Arendt, R. G., Kelsall, T., et al. 1998, ApJ, 508, 25
Houck, J. R., Roellig, T. L., van Cleve, J., et al. 2004, ApJS, 154, 18
Houck, J. R., Soifer, B. T., Weedman, D., et al. 2005, ApJ, 622, L105
Hummer, D. G. & Storey, P. J. 1987, MNRAS, 224, 801
Irwin, M. & Lewis, J. 2001, New Astronomy Review, 45, 105
Ivison, R. J., Smail, I., Le Borgne, J.-F., et al. 1998, MNRAS, 298, 583
Jenkins, A., Frenk, C. S., White, S. D. M., et al. 2001, MNRAS, 321, 372
Kennicutt, Jr., R. C. 1992, ApJ, 388, 310
Kennicutt, Jr., R. C. 1998, ARA&A, 36, 189
Kreysa, E., Gemuend, H.-P., Gromke, J., et al. 1998, in Advanced Technology MMW, Radio, and Terahertz Telescopes, ed T. G. Phillips, Proc. SPIE, 3357, 319
Lacy, M., Storrie-Lombardi, L. J., Sajina, A., et al. 2004, ApJS, 154, 166
Lonsdale, C., Farrah, D., & Smith, H. 2006, [arXiv:astro-ph/0603031]
Lonsdale, C., Polletta, M., Surace, J., et al. 2004, ApJS, 154, 54
Lonsdale, C. J., Smith, H. E., Rowan-Robinson, M., et al. 2003, PASP, 115, 897
Manners, J. C., Johnson, O., Almaini, O., et al. 2003, MNRAS, 343, 293
Manners, J. C., Serjeant, S., Bottinelli, S., et al. 2004, MNRAS, 355, 97
McMahon, R. G., Walton, N. A., Irwin, M. J., et al. 2001, New Astron. Rev., 45, 97
Mo, H. J. & White, S. D. M. 2002, MNRAS, 336, 112
Nagamine, K., Cen, R., Hernquist, L., Ostriker, J. P., & Springel, V. 2005, ApJ, 618, 23
Oke, J. B., Cohen, J. G., Carr, M., et al. 1995, PASP, 107, 375
Piovan, L., Tantalo, R., & Chiosi, C. 2003, A&A, 408, 559

Poggianti, B. M., Bressan, A., & Franceschini, A. 2001, ApJ, 550, 195
Polletta, M., Wilkes, B. J., Siana, B., et al. 2006, ApJ, 642, 673
Puget, J.-L., Abergel, A., Bernard, J.-P., et al. 1996, A&A, 308, L5+
Rieke, G. H., Young, E. T., Engelbracht, C. W., et al. 2004, ApJS, 154, 25
Rowan-Robinson, M. 2003, MNRAS, 345, 819
Rowan-Robinson, M., Lari, C., Perez-Fournon, I., et al. 2004, MNRAS, 351, 1290
Rowan-Robinson, M., Babbedge, T., Surace, J., et al. 2005, AJ, 129, 1183
Sanders, D. B., Salvato, M., Aussel, H., et al. 2007, astro-ph/0701318
Sawicki, M. 2002, AJ, 124, 3050
Shapley, A. E., Steidel, C. C., Pettini, M., & Adelberger, K. L. 2003, ApJ, 588, 65
Silva, L., Granato, G. L., Bressan, A., & Danese, L. 1998, ApJ, 509, 103
Simpson, C. & Eisenhardt, P. 1999, PASP, 111, 691
Soifer, B. T. & First Look Survey Team. 2004, in BAAS, 699
Somerville, R. S., Primack, J. R., & Faber, S. M. 2001, MNRAS, 320, 504
Stern, D., Eisenhardt, P., Gorjian, V., et al. 2005, ApJ, 631, 163
Surace, J. A., Shupe, D. L., Fang, F., et al. 2004, VizieR Online Data Catalog, 2255, 0
van Dokkum, P. G., Förster Schreiber, N. M., Franx, M., et al. 2003, ApJ, 587, L83
Veilleux, S. & Osterbrock, D. E. 1987, ApJS, 63, 295
Villar-Martin, M., Binette, L., & Fosbury, R. A. E. 1996, A&A, 312, 751
Weedman, D., Polletta, M., Lonsdale, C. J., et al. 2006, [arXiv:astro-ph/0608609]
Weisskopf, M. C., O'dell, S. L., & van Speybroeck, L. P. 1996, in Multilayer and Grazing Incidence X-Ray/EUV Optics III, ed. R. B. Hoover & A. B., Walker, Proc. SPIE 2805, 2
Werner, M. W., Roellig, T. L., Low, F. J., et al. 2004, ApJS, 154, 1
Yan, L., Chary, R., Armus, L., et al. 2005, ApJ, 628, 604

Online Material

Table 5. Results for first night. For each target, the number of detected absorption and emission lines is reported, as well as a photometric and spectroscopic (see footnotes) classification. The measured spectroscopic redshift is in Col. 6, while Col. 7 lists the photometric estimate of z, as obtained with the Hyper-z code (Bolzonella et al. 2000).

ID‡ SWIRE	RA J2000	Dec J2000	Det. Lines em.	abs.	z spec	z phot	Note*	Class† spec
LH_247176	162.9559600	57.8670580	0	0	–	0.720		–
LH_245141	162.9474900	57.8128240	1	0	1.017	0.890		ELG
LH_245572	162.9637900	57.8163990	1	0	0.935	0.890		ELG
LH_244996	162.9585700	57.8022500	0	0	–	1.240		–
LH_244783	162.9599600	57.7954600	0	0	–	0.590		–
LH_247598	163.0059200	57.8525350	0	0	–	1.130	P3L	–
LH_246388	163.0071900	57.8170200	2	0	0.700	1.030		ELG
LH_247704	163.0369100	57.8389550	1	0	0.419	0.500		ELG
LH_246801	163.0273900	57.8167570	0	0	–	1.420		–
LH_245973	163.0228400	57.7955510	0	0	–	2.840	P3L	–
LH_248065	163.0620100	57.8371960	0	0	–	1.000		–
LH_246098	163.0397000	57.7900430	1	0	0.927	0.400		ELG
LH_246660	163.0540000	57.7978250	0	0	–	2.780		–
LH_247451	163.0705900	57.8112640	0	0	–	1.790	P3	–
LH_245683	163.0602400	57.7662620	0	0	–	1.130		–
LH_245782	163.0663800	57.7654230	0	0	–	1.590	P2	–
LH_247597	163.0960800	57.8022120	0	0	–	1.780	P3	–
LH_247508	163.1037600	57.7950170	0	0	–	0.980		–
LH_247717	163.1172000	57.7946130	1	0	1.026	1.000		ELG
LH_248867	163.1425500	57.8190800	0	0	–	1.130		–
LH_246777	163.1230900	57.7627410	0	0	–	4.410		–
LH_574421	161.7675900	59.2445530	0	0	–	0.960		–
LH_571442	161.7003200	59.1992070	0	0	–	3.210	P3	–
LH_574156	161.7721700	59.2355310	0	0	–	1.000		–
LH_575325	161.8065900	59.2504010	5	0	0.355	0.310	X,R,pow	BLAGN
LH_574146	161.7805300	59.2307780	1	3	0.850	0.790		SB
LH_571907	161.7359900	59.1932950	5	0	0.504	1.400	R	SB
LH_571884 (s)	161.7322700	59.1946200	0	0	–	0.350		–
LH_574490	161.8032800	59.2278290	0	0	–	0.880		–
LH_574646	161.8123900	59.2275850	1	0	0.712	0.570	R	ELG
LH_572854	161.7723100	59.2003100	1	0	0.425	0.590		ELG
LH_572196	161.7604200	59.1882060	2	0	0.448	0.810		ELG
LH_572282	161.7674300	59.1873470	0	0	–	0.390		–
LH_573252	161.7947200	59.1993520	1	0	0.826	0.890	R	ELG
LH_572243	161.7809600	59.1789440	3	0	1.820	1.840	P2,X	NLAGN
LH_573752	161.8214400	59.1984940	1	0	0.871	1.060		ELG
LH_572227	161.7896100	59.1740110	0	0	–	0.780		–
LH_575068	161.8864300	59.2018550	0	0	–	1.690	P3L,R	–
LH_574218	161.8758100	59.1835670	1	0	1.169	1.080		ELG
LH_572289	161.8328600	59.1532900	1	0	0.992	1.120	R	ELG
LH_573719	161.8779400	59.1690940	0	0	–	1.240		–
LH_572257	161.8488600	59.1439320	3	1	0.249	2.170	P3,X	SB
LH_571738	161.8405300	59.1352350	0	0	–	1.210		–
LH_574364	161.9098200	59.1693080	1	0	1.474	1.550	P3,R	NLAGN
LH_572820	161.8769100	59.1450000	6	0	0.305	0.590		SB
LH_574495	161.9221600	59.1664850	0	0	–	1.200		–
LH_572108	161.8726800	59.1277350	1	0	1.019	0.880	R	ELG
LH_572670	161.8921700	59.1328200	0	0	–	1.070	R	–
EN1_203038	242.2878400	54.7196460	0	0	–	1.040		–
EN1_204462	242.3317600	54.7288320	0	0	–	1.310		–
EN1_206332	242.4030800	54.7331850	1	6	0.754	0.490		ELG
EN1_205851	242.3945300	54.7264710	0	0	–	1.100		–
EN1_203688	242.3373700	54.7072750	1	0	0.737	1.010		ELG
EN1_204660	242.3713100	54.7115440	4	7	0.630	0.550		SB
EN1_202683	242.3188800	54.6936190	5	0	0.498	0.550		SB
EN1_202789	242.3312800	54.6889000	0	0	–	0.910		–
EN1_204678	242.3887200	54.7020150	2	0	0.469	0.440		ELG
EN1_204710	242.3942400	54.6996460	0	3	0.874	1.100		ALG
EN1_204752 (s)	242.3934800	54.7009500	4	0	0.469	0.200		SB
EN1_202261	242.3306400	54.6766240	1	0	1.339	1.190	P2	ELG
EN1_205467	242.4294900	54.6975290	0	0	–	0.370	P3,X,pow	–
EN1_203073	242.3640000	54.6769600	0	0	–	0.710		–
EN1_203962	242.4050100	54.6756210	8	0	0.874	0.860	X	NLAGN
EN1_202756	242.3763400	54.6624410	6	0	3.005	2.720		BLAGN
EN1_204120	242.4209400	54.6700710	3	0	1.475	0.350	X,pow	BLAGN
EN1_202023	242.3639100	54.6516880	1	3	0.898	1.010		SB
EN1_205340	242.4640000	54.6744960	1	0	0.905	0.910		ELG

Table 5. continued.

ID‡ SWIRE	RA J2000	Dec J2000	Det. Lines em.	Det. Lines abs.	z spec	z phot	Note*	Class† spec
EN1_202047	242.3729400	54.6469380	1	5	0.661	0.550		SB
EN1_204124	242.4431600	54.6573910	1	0	0.901	1.070		ELG
EN1_202260	242.4011400	54.6365320	4	0	1.545	1.480	P2,X	BLAGN
EN1_205034	242.4857800	54.6545030	1	0	0.876	0.910		ELG
EN1_203525	242.4547000	54.6364940	2	0	0.265	0.210		ELG
EN1_201165	242.3914200	54.6144640	1	2	0.762	0.220	X,pow	SB
EN1_283675	244.1841300	55.6057700	1	0	1.138	0.870		ELG
EN1_284886	244.2396200	55.6035190	0	2	0.800	0.810		ALG
EN1_285168	244.2629100	55.5971790	0	2	0.798	0.920		ALG
EN1_282051	244.1426400	55.5912250	4	0	3.100	0.210	pow	BLAGN
EN1_281866	244.1489000	55.5828820	1	0	0.732	0.900		ELG
EN1_282887	244.1957600	55.5805400	0	0	–	1.370		–
EN1_283904	244.2396100	55.5787850	0	0	–	0.980		–
EN1_283549	244.2381300	55.5712430	1	0	1.119	1.100		ELG
EN1_282211	244.1892700	55.5676650	1	0	1.103	1.120		ELG
EN1_282263 (s)	244.2012600	55.5621000	1	0	0.808	0.720		ELG
EN1_282169	244.2009400	55.5596310	4	0	0.461	0.970		ELG
EN1_281970 (s)	244.2005200	55.5551800	1	0	0.807	0.580		ELG
EN1_282870	244.2621500	55.5409550	0	0	–	0.910		–
EN1_281341	244.2031100	55.5369150	1	0	0.868	0.880		ELG
EN1_279813	244.1436800	55.5324780	2	4	0.720	0.730		SB
EN1_279609	244.1402700	55.5297660	1	0	1.165	0.910		ELG
EN1_281524	244.2280600	55.5273400	0	0	–	1.370		–
EN1_282078	244.2602400	55.5226250	4	0	1.685	1.770	P3	BLAGN
EN1_280187	244.1820500	55.5190510	1	0	0.891	0.980		ELG
EN1_281722	244.2551400	55.5166890	1	0	1.211	1.770		ELG
EN1_279954	244.1842200	55.5119670	5	0	2.409	2.770	P3,pow	BLAGN
EN1_279984 (s)	244.1844600	55.5128000	2	0	0.718	0.700		ELG
EN1_281198	244.2435300	55.5091170	0	0	–	1.070		–
EN1_280713	244.2269600	55.5062330	1	0	1.211	1.420		ELG
EN1_280065 (s)	244.2111400	55.4988300	7	5	0.102	0.100		SB
EN1_279938	244.2106500	55.4962500	1	5	0.903	1.080		SB
EN1_279170	244.1830700	55.4936370	0	0	–	1.320		–
EN1_280103	244.2275200	55.4899600	1	0	1.171	0.980		ELG
EN2_275885	248.2923000	40.9753460	0	0	–	0.600		–
EN2_275543	248.2659500	40.9568060	6	7	0.392	0.210		SB
EN2_275226	248.3021100	40.9663580	4	0	1.710	1.670	P2	BLAGN
EN2_274748 (s)	248.3105500	40.9599700	–	–	0.000	–		star
EN2_274821	248.3091000	40.9605980	1	0	0.909	0.970		ELG
EN2_274735	248.3425600	40.9739490	5	0	2.605	2.690	pow	BLAGN
EN2_273908	248.2948200	40.9358180	0	0	–	2.840		–
EN2_273814	248.3073100	40.9395140	0	0	–	1.610		–
EN2_273717	248.3398600	40.9519620	3	0	1.800	3.050	P3	BLAGN
EN2_273639	248.3609200	40.9597550	1	6	0.704	0.720		SB
EN2_273300	248.3362700	40.9415890	1	0	0.987	1.710	pow	ELG
EN2_272775	248.3101800	40.9183240	5	4	0.384	0.170		SB
EN2_272288	248.3251800	40.9139370	1	5	0.787	0.700		SB
EN2_272228	248.3427700	40.9206160	0	0	–	1.550		–
EN2_271541	248.3325800	40.9015120	1	0	1.156	1.100		ELG
EN2_271345	248.3609800	40.9107890	0	0	–	0.410		–
EN2_271260	248.3783700	40.9168550	4	0	1.820	0.500	pow	BLAGN
EN2_270481	248.3485400	40.8865470	1	0	1.186	1.220		ELG
EN2_270623	248.4030900	40.9140590	0	0	–	1.470		–
EN2_270327	248.3833800	40.8986470	1	0	1.061	1.050		ELG
EN2_270081	248.3608400	40.8828390	1	0	1.187	1.100		ELG
EN2_270049	248.3937700	40.8965800	0	0	–	1.030		–
EN2_269695	248.4180800	40.9003180	0	0	–	1.800	P3	–
EN2_269090	248.3551200	40.8594930	1	0	1.062	0.720		ELG

‡: (s) indicates serendipitous sources;
*: pow = IRAC power-law SED; P3 = 5.8 μm peaker; P2 = 4.5 μm peaker;
L = upper limit at 8.0 μm; R = radio source; X = X-ray source.
†: ELG = emission lines; SB = starburst diagnostics; BLAGN = broad line AGN; NLAGN = narrow-line AGN; star = star; ALG = absorption lines only; nc = no continuum detected (but emission lines yes).

Table 6. Results for second night.

ID‡ SWIRE	RA J2000	Dec J2000	Det. Lines em.	Det. Lines abs.	z spec	z phot	Note*	Class† spec
LH_126754	164.5717500	57.8558810	0	0	–	2.950		–
LH_125952	164.5667600	57.8352280	0	0	–	2.140	P3L	–
LH_125107	164.5657700	57.8102190	1	0	0.974	1.090		ELG
LH_126739	164.5884700	57.8456920	0	0	–	1.040		–
LH_125753	164.5841200	57.8190310	0	0	–	0.910		–
LH_124994	164.5825700	57.7961500	0	0	–	1.160		–
LH_125213	164.5899700	57.7990530	5	0	0.477	0.210		SB
LH_125861	164.6013600	57.8122560	0	0	–	0.570		–
LH_128120	164.6321100	57.8646160	0	0	–	0.880		–
LH_127702	164.6326800	57.8511200	0	0	–	1.180		–
LH_127862	164.6456500	57.8481830	0	0	–	1.240		–
LH_128064	164.6524000	57.8508000	1	0	2.233	1.500	pow	ELG
LH_127481	164.6514900	57.8335190	1	0	0.854	0.740		ELG
LH_127839	164.6627500	57.8373490	0	0	–	0.950		–
LH_128218	164.6739800	57.8436010	1	0	0.932	1.370		ELG
LH_126546	164.6696800	57.7921940	0	0	–	1.920	P3L	–
LH_127562	164.6873800	57.8152280	1	0	1.200	1.320		ELG
LH_128115	164.6974900	57.8262560	1	0	0.741	0.860		ELG
LH_127706	164.7046700	57.8094410	1	0	0.965	0.970		ELG
LH_128777	164.7222900	57.8329660	0	0	–	2.140	P3	–
LH_129098	164.7355200	57.8357200	0	0	–	1.290		–
LH_129336	164.7433200	57.8387790	0	0	–	1.190		–
LH_129463	164.7498500	57.8388670	0	0	–	1.000		–
LH_129057	164.7492200	57.8263590	1	0	1.025	0.970		ELG
LH_128839	164.7504400	57.8182180	3	0	0.441	0.230		ELG
LH_127252	164.7381900	57.7757530	0	0	–	0.100		–
LH_129519	164.7719900	57.8275340	0	0	–	0.980		–
LH_129657	164.7800300	57.8278500	1	0	0.903	0.940		ELG
LH_129341	164.7840900	57.8150900	0	0	–	1.090		–
LH_573671	161.8165100	59.1993370	0	0	–	1.220		–
LH_576445	161.8730800	59.2471200	1	0	2.024	2.150	pow	ELG
LH_576161	161.8712900	59.2399900	1	0	0.988	0.970		ELG
LH_573414	161.8264300	59.1871410	1	4	0.749	0.980	R	SB
LH_573584	161.8378800	59.1861690	0	0	–	0.290		–
LH_576452	161.8964700	59.2355460	0	0	–	2.990		–
LH_573395	161.8467400	59.1762120	0	0	–	1.000		–
LH_577039	161.9206100	59.2402080	0	0	–	0.990		–
LH_575068	161.8864300	59.2018550	0	0	–	1.690	P3L,R	–
LH_577220	161.9356200	59.2369610	0	0	–	2.420	P3L,R	–
LH_574211	161.8810300	59.1807750	0	0	–	0.900		–
LH_577256	161.9487800	59.2319870	1	0	1.127	1.200		ELG
LH_576281	161.9357600	59.2106550	1	0	–	1.780	P2	ELG
LH_574939	161.9175900	59.1818120	0	0	–	1.810	P3L	–
LH_574364	161.9098200	59.1693080	3	0	1.474	1.550	P3,R	NLAGN
LH_576769	161.9698800	59.2069210	3	0	0.659	0.260	R,pow	ELG
LH_574561	161.9313400	59.1634520	0	0	–	1.130		–
LH_577480	161.9990700	59.2114450	1	0	0.581	0.800		ELG
LH_574430 (s)	161.9459800	59.1525500	0	0	0.000	–		star
LH_574491	161.9507600	59.1516720	0	0	–	0.500	pow	–
LH_575939	161.9877600	59.1729700	2	0	0.128	0.180		ELG
LH_576851	162.0119600	59.1873510	0	0	–	1.150		–
LH_576029 (s)	162.0022400	59.1681800	1	0	1.246	0.650		ELG
LH_575976	161.9977000	59.1693080	1	0	1.023	1.090		ELG
LH_577291	162.0328400	59.1889500	1	0	–	1.800	P3	–
LH_577043	162.0330000	59.1823390	0	0	–	0.970		–
EN1_344017	240.9222700	54.4750630	0	0	–	0.510		–
EN1_341502	240.8081500	54.4725880	7	0	2.317	2.910	pow	BLAGN
EN1_341999	240.8352800	54.4703790	0	0	–	1.220		–
EN1_343159	240.8965600	54.4654690	0	0	–	0.880		–
EN1_343609	240.9236000	54.4629630	0	4	0.547	0.390		ALG
EN1_342460	240.8772700	54.4583630	1	0	0.757	0.490		ELG
EN1_340789	240.8124200	54.4507180	1	0	1.092	0.480		ELG
EN1_341469	240.8508900	54.4476050	0	0	–	1.540	P3	–
EN1_343359	240.9443800	54.4448320	1	2	0.815	0.680		SB

Table 6. continued.

ID[‡]	RA	DEC	Det. Lines		z	z	Note[*]	Class[†]
SWIRE	J2000	J2000	em.	abs.	spec	phot		spec
EN1_342445	240.9084200	54.4407810	2	0	1.917	1.850	P3L	ELG
EN1_340451	240.8265700	54.4344670	3	0	2.866	2.320	P3	nc,NLAGN
EN1_340460	240.8344100	54.4303400	7	2	0.308	0.230		SB-LINER
EN1_341175	240.8745300	54.4267350	0	0	–	0.400		–
EN1_340982 (s)	240.8745000	54.4215800	0	0	–	–		–
EN1_340391	240.8643600	54.4120520	0	0	–	1.470		–
EN1_341090	240.9015500	54.4095340	1	6	0.586	0.470		SB
EN1_339716	240.8470200	54.4039960	4	4	0.637	0.940		SB
EN1_339960	240.8671700	54.3996240	2	0	1.475	1.590	P3	BLAGN
EN1_341304	240.9407700	54.3936770	–	–	0.000	–		star
EN1_339023	240.8445700	54.3869970	6	0	1.695	0.910		BLAGN
EN1_338063	240.8043800	54.3835910	0	0	–	0.990		–
EN1_339817	240.8988300	54.3781200	0	0	–	0.600		–
EN1_337826	240.8112900	54.3739470	7	0	1.756	1.760	pow	BLAGN
EN1_337232	240.8093400	54.3592490	2	4	0.796	0.730		SB
EN1_336978	240.8049600	54.3552630	1	0	1.221	0.230	pow	ELG
EN2_13210	250.416110	40.816822	1	0	0.198	0.450	pow	ELG
EN2_11561	250.406220	40.777615	0	0	–	0.950		–
EN2_12428	250.419310	40.801735	1	0	2.338	2.430		ELG
EN2_11247 (s)	250.416850	40.774560	4	0	0.442	0.410		SB
EN2_11160	250.420200	40.774158	0	0	–	1.210		–
EN2_11438	250.426320	40.783157	2	3	0.439	0.510		SB
EN2_11745	250.440830	40.796204	0	2	1.561	1.010		ALG
EN2_12554	250.451480	40.817425	1	4	1.886	0.970		SB
EN2_10334	250.438280	40.763359	–	–	–	2.010	P3	–
EN2_11850	250.456920	40.805145	0	0	–	1.270		–
EN2_11775 (s)	250.460020	40.805050	–	–	0.000	–		star
EN2_9745	250.448960	40.7555730	1	0	1.086	1.190		ELG
EN2_11091	250.464570	40.791348	1	0	1.946	2.140	P3L	ELG
EN2_11749	250.480210	40.812843	1	7	0.776	1.150		SB
EN2_10010	250.480990	40.773952	1	3	0.673	0.960		SB
EN2_10278	3250.493590	40.785378	5	0	1.720	1.020	pow	BLAGN
EN2_8495	250.4924500	40.7474290	6	7	0.362	0.110		SB
EN2_10015	250.508500	40.786121	0	7	0.737	0.710		ALG
EN2_9634	250.5140400	40.7809330	0	0	–	1.200		–
EN2_8917	250.5139000	40.7654500	0	2	0.802	0.710		ALG
EN2_8175	250.5173800	40.7505040	2	0	0.479	0.330		ELG
EN2_9885	250.5391700	40.7966540	1	8	0.875	0.780		SB
EN2_9757	250.5478500	40.7976260	0	0	–	0.100		–
EN2_8936	250.5501900	40.7812420	1	3	0.718	0.880		SB
EN2_6835	250.5366800	40.7290000	1	0	1.400	1.320		ELG
EN2_6702	250.5427900	40.7288020	1	3	0.916	0.980		SB
EN2_9202	250.5687000	40.7944600	1	7	0.671	0.590		SB
EN2_172324	248.6213800	41.0597310	4	0	1.739	2.070	P3	NLAGN
EN2_172031	248.6326600	41.0595360	4	7	0.558	0.780		SB
EN2_170417	248.6353800	41.0304950	0	0	–	1.150		–
EN2_170393	248.6875600	41.0532300	1	0	0.912	1.070		ELG
EN2_169884	248.6255800	41.0156140	1	8	0.581	0.580		SB
EN2_169626	248.6974500	41.0424770	0	0	–	0.300		–
EN2_168961	248.6883400	41.0261760	0	0	–	0.490		–
EN2_168666	248.6705200	41.0127720	1	0	1.205	0.990		ELG
EN2_168355	248.6358200	40.9916650	1	0	0.952	0.490		ELG
EN2_167372	248.6506800	40.9797590	1	0	1.445	2.120	P2L	ELG
EN2_167270 (s)	248.6517500	40.9784900	0	0	–	1.270		–
EN2_167232	248.6960300	40.9974060	5	8	0.522	0.290		SB
EN2_166853	248.6574900	40.9735030	1	4	0.909	0.890		SB
EN2_166134	248.6786000	40.9687960	1	0	1.337	1.470	P2	ELG
EN2_165986	248.7120400	40.9809680	4		2.163	0.430	P3,pow	BLAGN
EN2_165843	248.7228500	40.9832570	0	0	–	0.990		–
EN2_165571 (s)	248.7258800	40.9798900	1	5	0.797	0.100		SB

[‡]: (s) indicates serendipitous sources;
[*]: pow = IRAC power-law SED; P3 = 5.8 μm peaker; P2 = 4.5 μm peaker;
L = upper limit at 8.0 μm; R = radio source; X = X-ray source.
[†]: ELG = emission lines; SB = starburst diagnostics; BLAGN = broad line AGN; NLAGN = narrow-line AGN; star = star; ALG = absorption lines only; nc = no continuum detected (but emission lines yes).

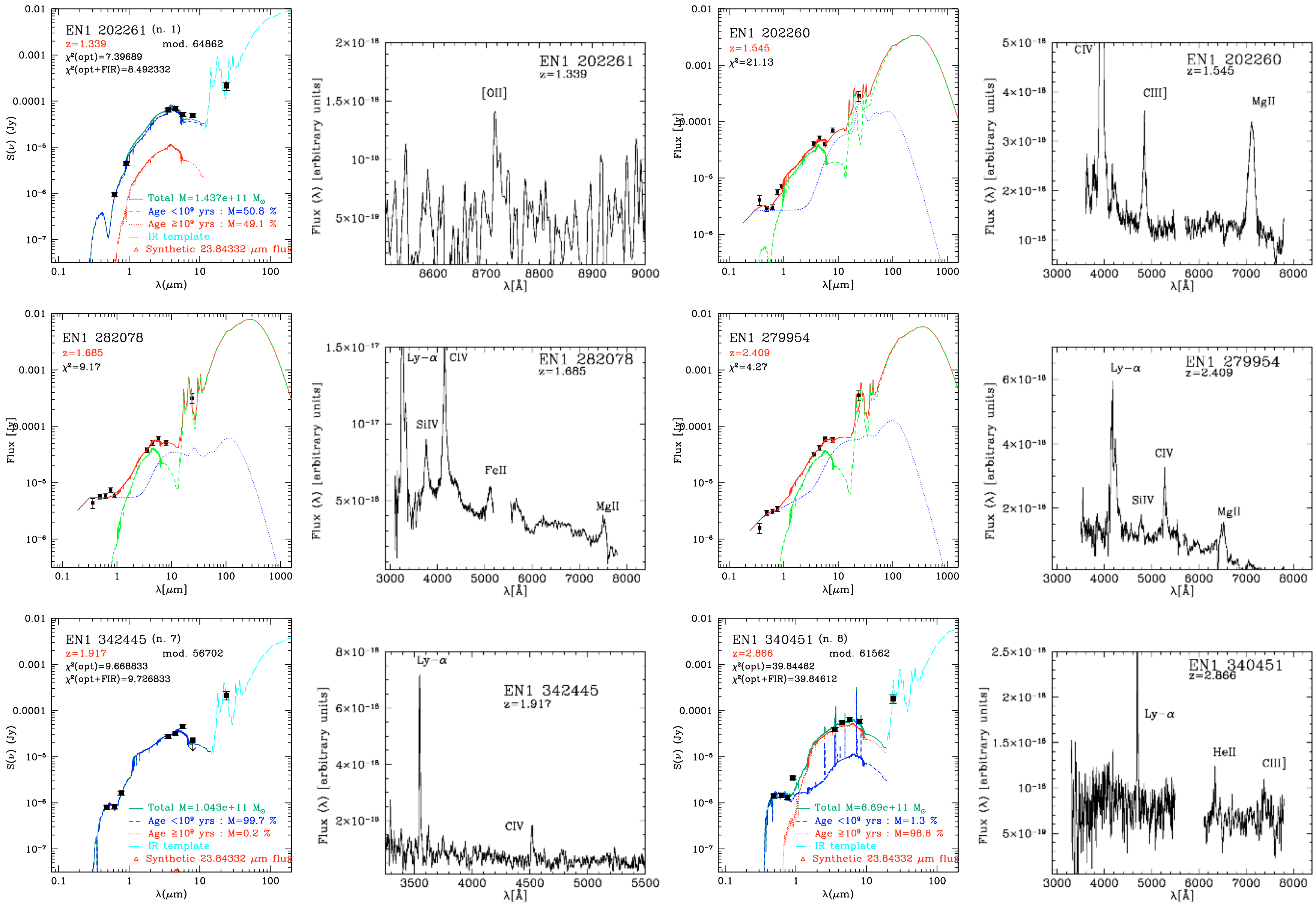

Fig. 7. IR-peak sources with spectroscopic redshift: broad band SEDs and spectra. Sources with no AGN detected in the UV-optical spectra are fitted with spectrophotometric synthesis (Berta et al. 2004). In these cases, the dotted lines represent old (age $\geq 10^9$ yr) stellar populations, dashed lines are younger stars, the dashed lines long ward 5 μm (restframe) are the IR starburst template adopted (see text) and the solid lines are the total best fit. χ^2 values computed without accounting ("opt") and accounting ("opt+FIR") for the available 24 μm flux are reported. If an AGN was detected, a multi-component fit is performed. In these cases, the dashed lines are the stellar + starburst dust component, the dotted lines represent the torus model and the solid lines are the sum of the two. A unique χ^2 value is derived, taking into account all the available data.

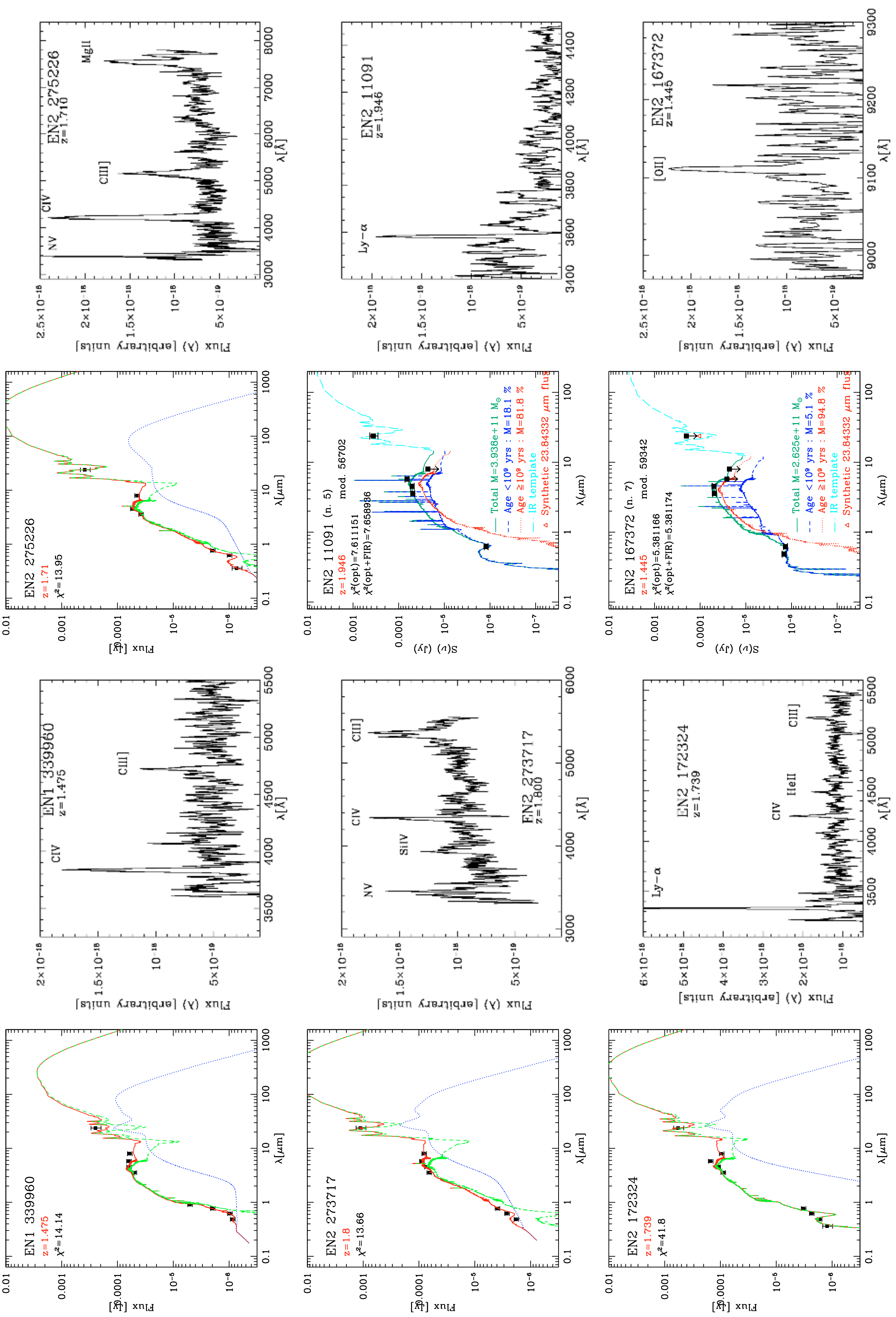

Fig. 7. continued.

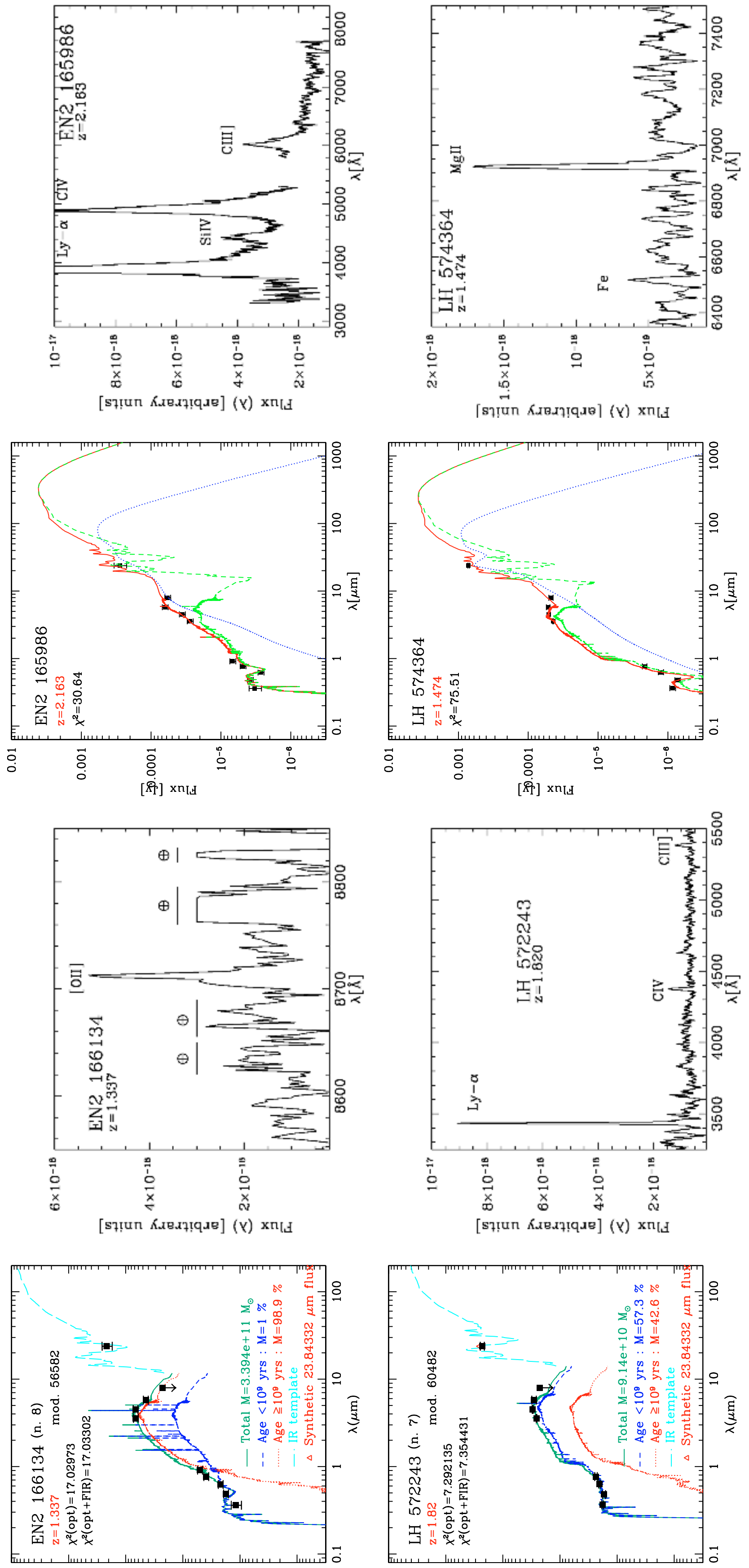

Fig. 7. continued.